

UCLA

UCLA Previously Published Works

Title

The Faustini Permanently Shadowed Region on the Moon

Permalink

<https://escholarship.org/uc/item/6mz6r9b0>

Journal

The Planetary Science Journal, 5(9)

ISSN

2632-3338

Authors

Williams, Jean-Pierre

Mahanti, Prasun

Robinson, Mark S

et al.

Publication Date

2024-09-01

DOI

10.3847/psj/ad6f0d

Copyright Information

This work is made available under the terms of a Creative Commons Attribution License, available at <https://creativecommons.org/licenses/by/4.0/>

Peer reviewed



The Faustini Permanently Shadowed Region on the Moon

Jean-Pierre Williams¹ , Prasun Mahanti² , Mark S. Robinson² , Robert V. Wagner² , Marley Chertok^{3,4} ,
 Norbert Schörghofer⁵ , Erwan Mazarico⁶ , Brett W. Denevi⁷ , Shuai Li⁴ , and David A. Paige¹

¹ Department of Earth, Planetary, and Space Sciences, University of California, Los Angeles, Los Angeles, CA 90095, USA; jpierre@mars.ucla.edu
² School of Earth and Space Exploration, Arizona State University, Tempe, AZ 85287, USA
³ Department of Earth and Planetary Sciences, University of Hawaii at Mānoa, Honolulu, HI 96822, USA
⁴ Hawaii Institute of Geophysics and Planetology, Honolulu, HI 96822, USA
⁵ Planetary Science Institute, Tucson, AZ 85719, USA
⁶ NASA Goddard Space Flight Center, Greenbelt, MD 20771, USA
⁷ Johns Hopkins University Applied Physics Laboratory, Laurel, MD 20723, USA

Received 2024 June 14; revised 2024 August 10; accepted 2024 August 12; published 2024 September 25

Abstract

Faustini crater (41 km diameter) hosts a large (664 km²) permanently shadowed region (PSR) with a high potential to harbor water-ice deposits. One of the 13 candidate Artemis III landing areas contains a portion of the crater rim and proximal ejecta. The ShadowCam instrument aboard the Korea Pathfinder Lunar Orbiter provides detailed images of the PSR within Faustini. We characterize the terrain and thermal environment within the Faustini PSR from ShadowCam images, Lunar Reconnaissance Orbiter thermal measurements and laser ranging, and thermal modeling. Our mapping revealed three distinct areas of the floor of Faustini based on elevations, slopes, and surface roughness. These units broadly correlate with temperatures; thus, they may be influenced by variations in volatile sublimation. Crater retention and topographic diffusion rates appear to be asymmetric across the floor, likely due to differences in maximum and average temperatures. Several irregular depressions and a pronounced lobate-rim crater are consistent with subsurface ice. However, differences in the thicknesses of deposited materials on the floor may also explain the asymmetry. Additionally, zones of elevated surface roughness across Faustini appear to result from overprinted crater ray segments, possibly from Tycho and Jackson craters. Mass wasting deposits and pitting on opposite sides of the crater wall may have resulted from the low-angle delivery of material ejected by the Shackleton crater impact event, suggesting that the Artemis III candidate landing region named “Faustini Rim A” will contain material from Shackleton.

Unified Astronomy Thesaurus concepts: [The Moon \(1692\)](#); [Lunar regolith \(2315\)](#); [Lunar surface \(974\)](#); [Lunar science \(972\)](#); [Lunar features \(953\)](#)

1. Introduction

Some areas within lunar polar regions are permanently shadowed from direct solar illumination due to the low obliquity of the lunar spin axis relative to the ecliptic plane, $\sim 1^\circ.54$ (e.g., K. Watson et al. 1961; J. R. Arnold 1979; D. A. Paige et al. 1992; D. B. J. Bussey et al. 1999; J. L. Margot et al. 1999; D. B. J. Bussey et al. 2003; E. Mazarico et al. 2011). These permanently shadowed regions (PSRs) can experience some of the lowest temperatures observed in the solar system (D. A. Paige et al. 2010b; D. A. Paige & M. A. Siegler 2016). Within PSRs, heat radiated to space is offset only by scattered indirect illumination and thermal emission by nearby surfaces and, to a lesser extent, residual heat from the lunar interior, and in some areas intermittent earthshine (A. P. Ingersoll et al. 1992; D. A. Paige et al. 1992; J. R. Salvail & F. P. Fanale 1994; A. Vasavada 1999; D. A. Paige et al. 2010b). Temperatures vary both seasonally and diurnally due to the expansion and contraction of shadowed areas with seasons that can have a substantial influence on the amount of light scattered into PSRs (J.-P. Williams et al. 2019; J. L. Kloos et al. 2019; N. Schörghofer & J.-P. Williams 2020; N. Schörghofer et al. 2024).

The lunar polar regions are a high priority for science and exploration, as the low temperatures within PSRs result in cold

traps for water and other volatile species, and many of the regions have experienced cryogenic temperatures for over a billion years (M. Siegler et al. 2015; N. Schörghofer & R. Rufu 2023). In this paper, we characterize the terrain properties and thermal environment within the Faustini crater PSR (Figure 1) using Korea Pathfinder Lunar Orbiter (KPLO/Danuri) ShadowCam images, along with elevation and temperature data from the Lunar Reconnaissance Orbiter (LRO) Lunar Orbiter Laser Altimeter (LOLA) and Diviner instruments and temperatures derived from thermal modeling. Faustini is a 41 km wide impact crater, and the 664 km² PSR contained within it is the third-largest lunar PSR. The PSR is estimated to have a high potential to harbor water ice (H. M. Brown et al. 2022) and is overlapped by one of the 13 candidate Artemis III landing regions (Faustini Rim A; NASA-Press 2022).

2. Background

Water molecules likely migrate in the lunar environment through a series of ballistic hops in the surface-bound exosphere (K. Watson et al. 1961; J. R. Arnold 1979), and hydration (OH/H₂O) has been detected on the lunar surface and exosphere (C. M. Pieters et al. 2009; J. M. Sunshine et al. 2009; R. N. Clark 2009; R. Sridharan et al. 2010; A. R. Hendrix et al. 2012; C. I. Honniball et al. 2020, 2021). The residence time of a water molecule decreases exponentially with surface temperature, and molecules landing in a PSR can become trapped on gigayear timescales and accumulate, as temperature-

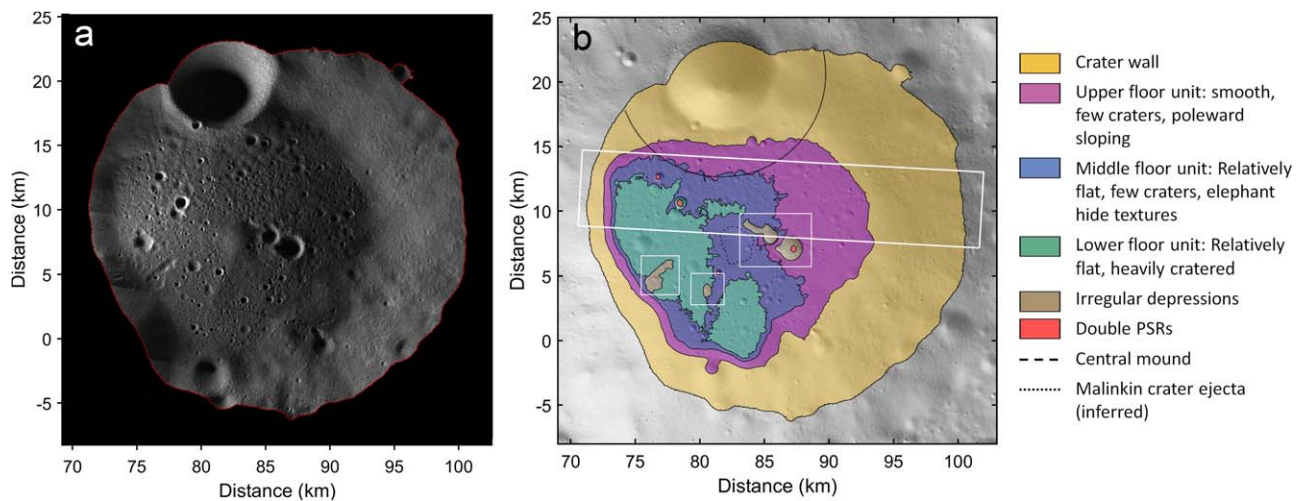


Figure 1. (a) ShadowCam mosaic of the Faustini PSR composed of images acquired during 2023 January and February. The Sun direction is to the right. (b) Geomorphic map highlighting terrain features within the PSR. Axes are distances from the South Pole (left sides of panels are the poleward side). The larger white box is the location of the ShadowCam image in Figures 4 and 14, and smaller white boxes are locations of Figure 10(a)–(b), 10(c)–(d), and 10(e)–(f) (left to right). The lunar nearside is toward the top of the panel.

dependent sublimation rates can be exceedingly low (e.g., N. Schörghofer 2022; B. Teolis et al. 2023; N. Schörghofer & J.-P. Williams 2024). Observations have confirmed that water is present in the polar regions, though the concentrations and distributions of the water have remained uncertain (see, e.g., D. J. Lawrence 2017; P. G. Lucey et al. 2022; J.-P. Williams & L. Rubanenko 2024, for reviews).

Neutron spectroscopy from the Lunar Prospector mission (W. C. Feldman et al. 1998) and the LRO Lunar Exploration Neutron Detector (LEND; I. G. Mitrofanov et al. 2010) show a suppression of neutrons at the poles consistent with an enhancement of hydrogen with the largest neutron suppression areas overlying PSRs (W. C. Feldman et al. 2000, 2001; R. C. Elphic et al. 2007; V. R. Eke et al. 2009; L. F. A. Teodoro et al. 2010). The Lunar Crater Observation Sensing Satellite (LCROSS; A. Colaprete et al. 2012) kinetic impact experiment confirmed the presence of water and other volatile species in the Cabeus PSR (A. Colaprete et al. 2010; G. R. Gladstone et al. 2010; P. H. Schultz et al. 2010; P. O. Hayne et al. 2010; D. M. Hurley et al. 2012; K. M. Lucchinger et al. 2021).

The LRO Diviner Lunar Radiometer Experiment (Diviner; D. A. Paige et al. 2010a) has been collecting global brightness temperature measurements near-continuously since mid-2009 (J.-P. Williams et al. 2017), revealing polar temperature variations, both diurnally and seasonally (D. A. Paige et al. 2010b; J.-P. Williams et al. 2019). These temperature observations have been used to map the thermal stability of both surface and subsurface water-ice stability and other volatile species (D. A. Paige et al. 2010b; N. Schörghofer & J.-P. Williams 2020; N. Schörghofer et al. 2021; M. E. Landis et al. 2022; N. Schörghofer & J.-P. Williams 2024; N. Schörghofer et al. 2024). Several lines of evidence have suggested that water ice may be exposed at the surface within regions where water is predicted to be stable. Observations from the LRO Lyman Alpha Mapping Project (LAMP) instrument show reflectance and spectral characteristics consistent with surface water ice (G. R. Gladstone et al. 2012; P. O. Hayne et al. 2015), and reflectance measurements at 1064 nm by LOLA also show a contrast in reflectance in these regions (E. A. Fisher et al. 2017; L. Qiao et al. 2019). Many of these areas also exhibit

near-infrared spectral features diagnostic of water using Chandrayaan-1 Moon Mineralogy Mapper (M3) data (S. Li et al. 2018); however, evidence for surface exposures of ice is not found at all locations where cold trapping can occur.

Radar observations also hinted at the possibility of ice deposits (P. D. Spudis et al. 2010, 2013; G. W. Patterson et al. 2017); however, the interpretation of radar observations as ice detections is ambiguous, as both icy deposits and rocky materials can generate similar radar backscatter and polarization characteristics for a given phase angle (B. A. Campbell 2012; A. Virkki & K. Muinonen 2016). Young impact craters are characterized by rough, blocky surface texture on their ejecta and interiors that result in high circular polarization ratio (CPR) signatures (e.g., S. Nozette et al. 2001; D. B. Campbell et al. 2006). A class of craters with high CPR values only within their interior in the polar regions have been suggested to result from ice within the crater interiors (P. D. Spudis et al. 2010, 2013), though craters with similar CPR characteristics have been noted in nonpolar areas (W. Fa & V. R. Eke 2018).

Long-exposure images acquired by the Lunar Reconnaissance Orbiter Camera (LROC) Narrow Angle Camera (NAC) within many of the PSRs provided images of their interiors at pixel scales of ~ 10 – 40 m (S. D. Koeber et al. 2014; E. Cisneros et al. 2017). Additionally, B. Moseley et al. (2021) have developed a deep-learning-based method to remove noise from full-resolution NAC images within PSRs resolving features as small as ~ 3 m. Reflectance anomalies or boundaries attributable to surface frost or exposures of ice were not identified in either the long-exposure images (H. M. Brown et al. 2022) or the denoised images (V. T. Bickel et al. 2021, 2022); however, it has been suggested that some regions where water ice is thermally stable appear smooth relative to warmer surfaces, possibly the result of terrain softening due to the presence of ice (A. N. Deutsch et al. 2021; S. Moon et al. 2021).

The ShadowCam instrument on board the KPLO spacecraft is now providing information regarding the landform morphology and reflectance of PSRs at exploration scales (< 10 m), yielding additional insight into the lunar polar terrains (M. S. Robinson et al. 2023). The instrument was designed to provide high-resolution (pixel scale of 1.7 m) and high signal-to-noise ratio (typically > 100) images under the low-light

conditions experienced within the PSRs (D. C. Humm et al. 2023). The camera has a high heritage from the LROC NAC (M. S. Robinson et al. 2010) instrument. Modifications to the design include a time delay integration sensor providing 200 times greater sensitivity, and improved stray light mitigation increasing the image signal-to-noise ratio.

3. Data and Methods

3.1. ShadowCam

ShadowCam has completed its 1 yr primary mission and continues to acquire images in an extended mission, providing images of PSRs through an entire draconic year. The mission began after achieving its 100 km mission orbit on 2022 December 27 (M.-J. Jeon et al. 2024) during southern summer, when illumination conditions were optimal for high signal-to-noise ratio in the southern hemisphere. Over 150 images were collected during the month-long commissioning phase and primary mission that overlapped the Faustini PSR. ShadowCam images were processed using ISIS3 software to apply radiometric calibrations (D. C. Humm et al. 2023) and map-project the data. All images were projected in polar stereographic at 2 m pixel^{-1} onto a 30 m pixel^{-1} digital elevation model (DEM) derived from LOLA data (D. E. Smith et al. 2010). A mosaic of the Faustini PSR was generated using images acquired from 2023 January and February at a pixel scale of 2 m and is shown in Figure 1. The mosaic was examined using ArcGIS and QGIS to identify surface features (craters, boulders, scarps, etc.) and textures (e.g., elephant hide terrains). Crater counting was conducted using the ArcMap and QGIS plugins Cratertools (T. Kneissl et al. 2011) and OpenCraterTool (T. Heyer et al. 2023). Crater diameters were measured down to 10 m diameter in three regions of the crater floor that were representative of morphologic terrain types identified in this study (Section 4).

3.2. Topography

The enhanced south polar DEMs derived from LOLA (M. K. Barker et al. 2023) were used to characterize elevation, slopes, and surface roughness. Surface roughness was quantified using the vector ruggedness measure (VRM; R. D. Hobson 1972; J. M. A. R. K. Sappington et al. 2007), which characterizes the dispersion of normal vectors of grid cells within a window capturing the variability of slope and aspect in a single metric. Slope and aspect are decomposed into x , y , and z components using standard trigonometric operators and summed to calculate the magnitude of the resultant vector for a 3×3 -pixel moving window. Dividing the resultant vector by the number of cells in the window and subtracting from 1 provides a dimensionless number between 0 (completely flat) and 1 (maximum terrain variation). VRM decouples roughness from slope better than other commonly employed roughness indices, such as the terrain ruggedness index (TRI; S. J. Riley et al. 1999; see Figure 2), and has been employed previously in the lunar polar regions to compare surface roughness in and around water-ice stability areas (A. N. Deutsch et al. 2021). Additional roughness indices such as a slope-detrended TRI (a best-fit plane at the desired length scale is subtracted; M. K. Barker et al. 2023; L. O. Magaña et al. 2024) and the standard deviation of slopes (K. L. Frankel & J. F. Dolan 2007; S. Moon et al. 2021) also provide a roughness metric that is decoupled from regional slope and yields qualitatively similar

results to VRM. The VRM was calculated using three DEM sampling scales (20, 40, and 80 m) to characterize roughness at three different spatial scales. Roughness variations are observed to be heavily dominated by impact cratering. To increase the detail of other textural variations and enhance the contrast in the maps, VRM values were linearly mapped to values between 0 and 1; saturation of the top and bottom 1% of the values and contrast-limited adaptive histogram equalization (S. M. Pizer et al. 1987) were applied (Figure 3).

3.3. Temperatures

Maximum and average temperatures of the Faustini PSR were mapped using Diviner bolometric temperatures (240 m pixel^{-1} south polar stereographic grids; J.-P. Williams et al. 2019). The gridded data represent the cumulative nadir-pointing observations from 2009 July 5 to 2019 February 17. The seasonal and diurnal coverage of Diviner is not complete, and the instrument no longer observes Faustini owing to the migration of the LRO spacecraft orbit (E. Mazarico et al. 2018). Thus, we used a thermal model to provide temperature estimates at higher temporal and spatial resolutions. The thermal model is based on D. A. Paige et al. (2010b) and accounts for topography (240 m scale triangular mesh) and direct and indirect infrared and visible radiation in the thermal balance of the regolith. Each triangle of the mesh is coupled to a regolith thermal model (A. Vasavada 1999). There is generally good agreement between maps and histograms of modeled and observed bolometric temperatures (D. A. Paige et al. 2010b; J.-P. Williams et al. 2023a, 2023b). Temperatures were modeled for a 2 yr period starting with the beginning of the KPLO mission (2023 January), allowing for a direct comparison of temperatures with ShadowCam radiance values. The model was run for a 20 yr span (years 2003–2023) prior to outputting results to ensure that the model had thermally equilibrated and no secular drift in the temperatures was occurring.

3.4. Sublimation Rates

Cold traps of the volatile species identified by the Lunar Crater Observation and Sensing Spacecraft (LCROSS) impact experiment (A. Colaprete et al. 2010) have been mapped for the south polar region of the Moon. N. Schörghofer & J.-P. Williams (2020, 2024) and N. Schörghofer et al. (2021) used sublimation rates time-averaged over diurnal and seasonal cycles from Diviner-derived temperatures to map cold trapping regions poleward of 80° south latitude. These maps were used to evaluate the cold trapping regions of several volatile species within the Faustini PSR.

4. Results

4.1. Elevation, Slope, and Surface Roughness

We subdivided the floor of Faustini into three regions based on elevation, break-in-slope, and differences in surface roughness and textures; unit transitions generally correspond to the elevation contours of -2710 and -2740 m (Figure 3). We use these contours to delineate Upper, Middle, and Lower Floor units (Figure 1(b)). The floor is generally sloped poleward from an elevation of -2600 m down to $\sim -2770 \text{ m}$, with the interiors of depressions and impact craters extending

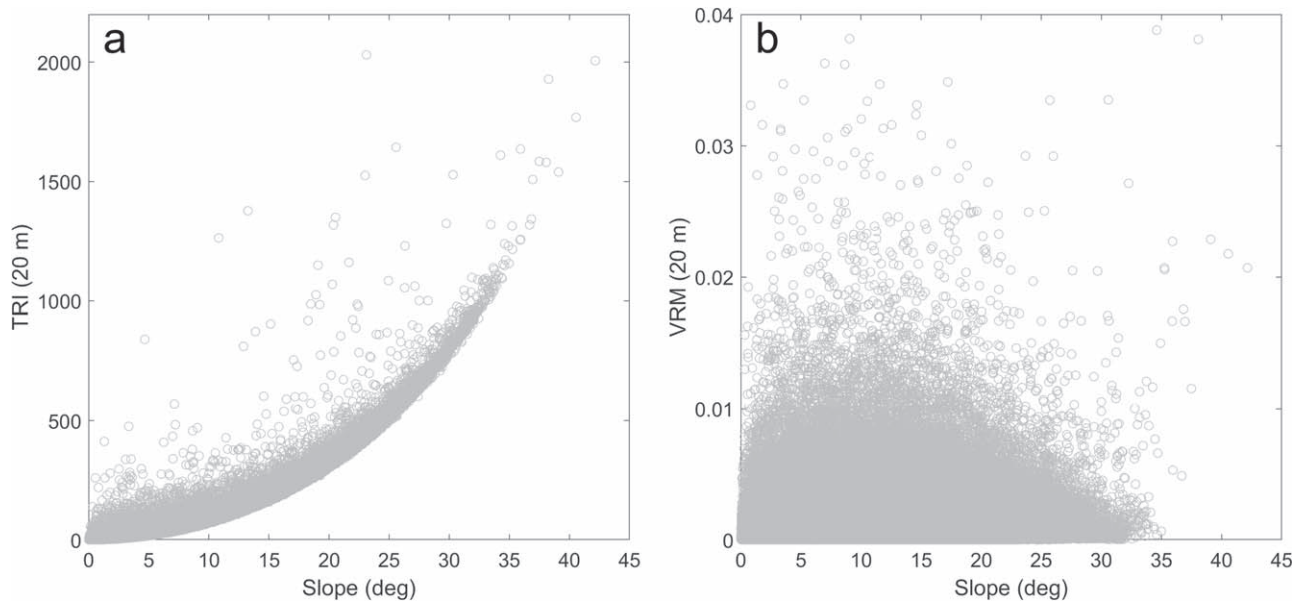


Figure 2. Scatter plots of surface roughness indices (a) TRI and (b) VRM vs. slope using the 20 m pixel⁻¹ DEM from M. K. Barker et al. (2023) for the region in Figure 1(b).

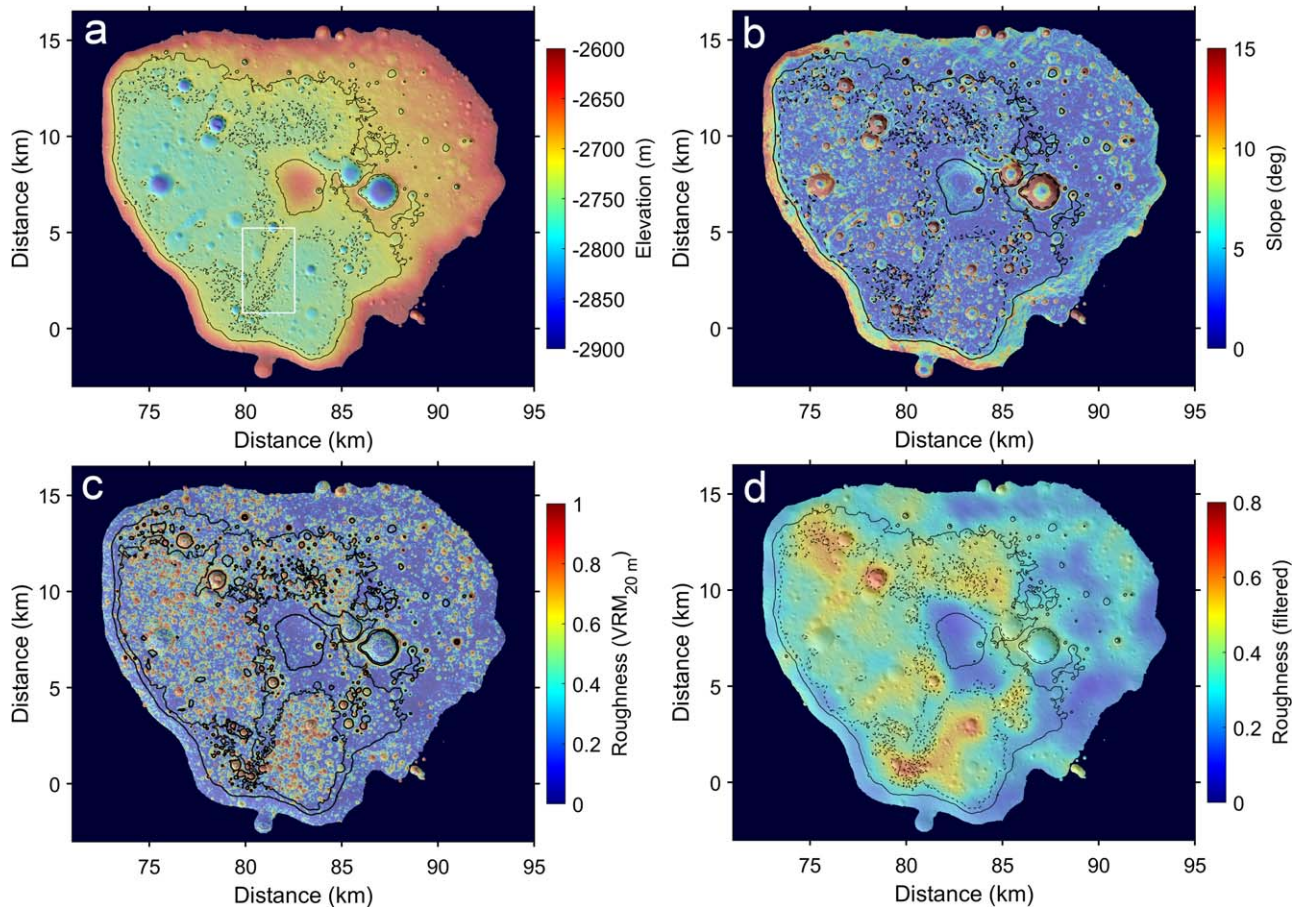


Figure 3. Shaded relief maps of the floor of Faustini crater derived from the 20 m pixel⁻¹ DEM (M. K. Barker et al. 2023) showing (a) elevation, (b) slope, (c) roughness, and (d) roughness filtered with a Gaussian-weighted moving average. Contours are elevations -2740 and -2710 m. The white box in panel (a) is the location of Figure 5.

deeper, with the lowest elevation, -2900 m, occurring within the largest crater ($D = 2$ km).

Figure 3(a) shows the shaded relief of the Faustini floor for all elevations below -2600 m colored with elevation.

Malinkin crater, a ~ 8.5 km crater superposed on the wall of Faustini in the upper portion of Figure 1, has not been included, though portions of Malinkin crater's interior are below -2600 m. The Upper Floor unit, defined here as floor

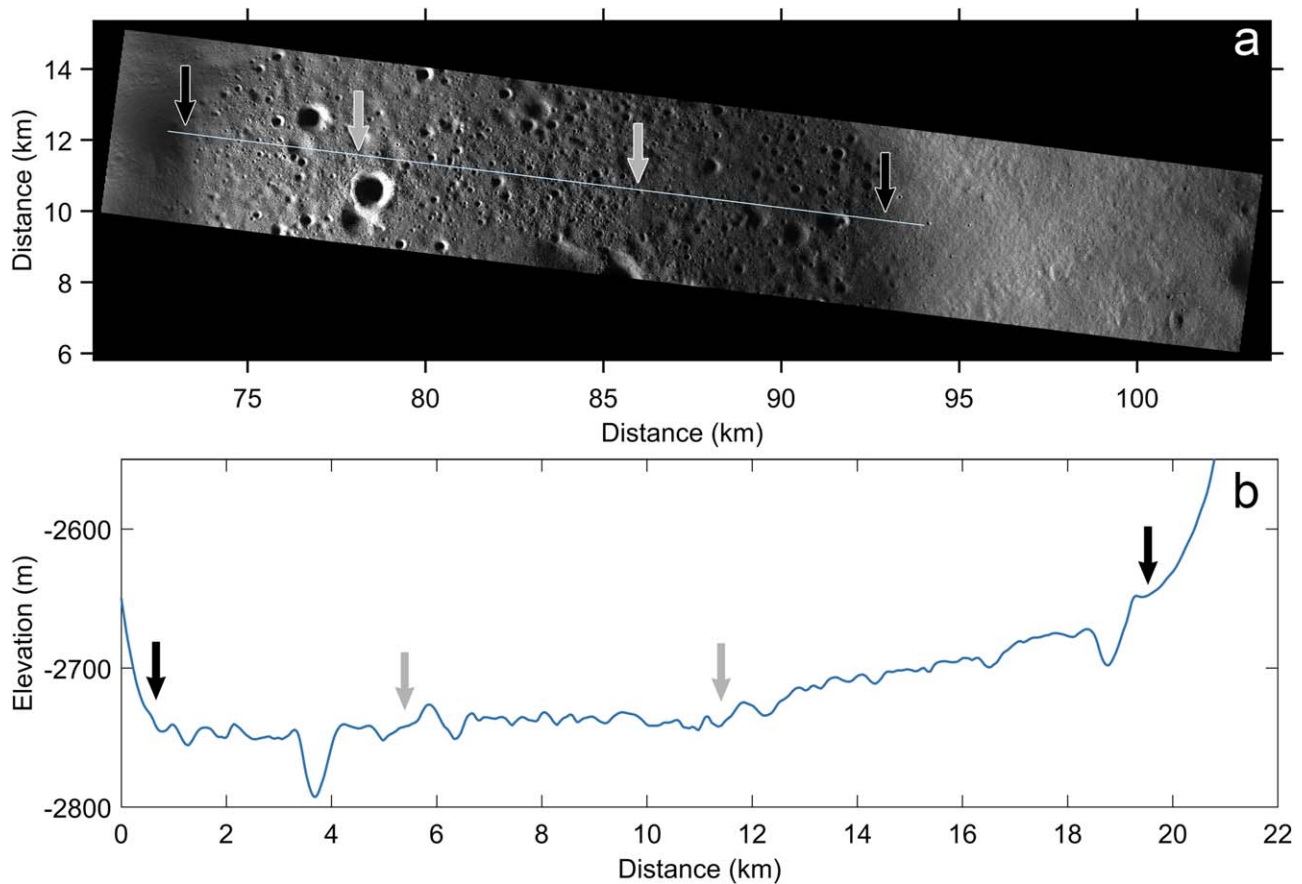


Figure 4. (a) ShadowCam image M15308992S; (b) elevation profile across Faustini floor. The location of the image is shown in Figure 1(b). The line in panel (a) shows the location of the elevation profile. Black arrows denote the wall/floor contacts, and gray arrows are the locations of transitions between Upper and Middle (right) and between Middle and Lower (left) morphologic units in Figures 1(b) and 6(a).

elevations between -2600 and -2710 m, largely composes the equator-side (lower-latitude side) of the floor and is generally sloped poleward (Figure 4). Material ejected during the formation of Malinkin likely superposes a portion of the floor (top of Figure 1(b)) contributing to the topographic gradient in this area. The Middle Floor unit between -2710 and -2740 m is comparatively flat, with the exception of impact craters and depressions and a broad mound at the center of the floor with ~ 55 m of relief above the -2710 m elevation, which may be the remnant of a degraded central peak. The Lower Floor unit, which extends below -2740 m, is also relatively flat and composes the poleward half of the floor. The Lower Floor unit is separated into two portions by a low, broad ridge extending from the central mound. Portions of the ridge contain scarps morphologically similar to lobate thrust fault scarps, suggesting that the ridge may be tectonic in origin and represent a previously unknown ~ 4 km lobate scarp (Figure 5; A. Mishra & P. Senthil Kumar 2022; T. R. Watters et al. 2024).

The surface roughness, defined with VRM at three length scales (20, 40, and 80 m pixel $^{-1}$), shows that the Lower unit is rough compared to the Upper unit and the Middle unit around the central mound, a distribution consistent with roughness mapping by L. O. Magaña et al. (2024). Areas of the Middle unit that are more distal to the central mound are disrupted by heavily degraded craters, resulting in elevated roughness in the maps. Figure 3(c) shows the VRM using the 20 m pixel $^{-1}$ DEM. Values have been scaled and contrast enhanced as described in Section 3.2. Figure 3(d) shows the same data

filtered with a Gaussian-weighted moving average highlighting the regional variation in roughness on the floor. A histogram of the original (i.e., not contrast enhanced) VRM values highlights the differences in the distribution of surface roughness values between the different elevations, with roughness increasing with decreasing elevation of the units (Figure 6). The VRM values of the three length scales are combined into an RGB composite to highlight the roughness at the different length scales, where roughness at shorter length scales is blueshifted and that at longer length scales is redshifted (Figure 7). The Middle unit appears comparatively smooth on and around the central mound at all three length scales compared to the rest of the floor. The Upper unit also appears smoother than the remaining Middle unit and Lower unit. The Middle unit represents a narrow range of elevations (30 m) forming a relatively flat bench of topography that is disrupted by impacts, making it appear rough in places. The Lower unit contains the greatest density of elevated VRM values.

4.2. Impact Craters and Surface Textures

Impact craters appear to be the primary contributor to the elevated VRM values, with variations in crater densities largely responsible for the differences in the distributions of VRM values between the units. Crater counts conducted on representative areas of the three units show variations in the crater size–frequency distributions (CSFDs; Figure 8). Craters down to $D = 10$ m were measured, and a greater density of craters was observed on the Lower unit, where the CSFD was

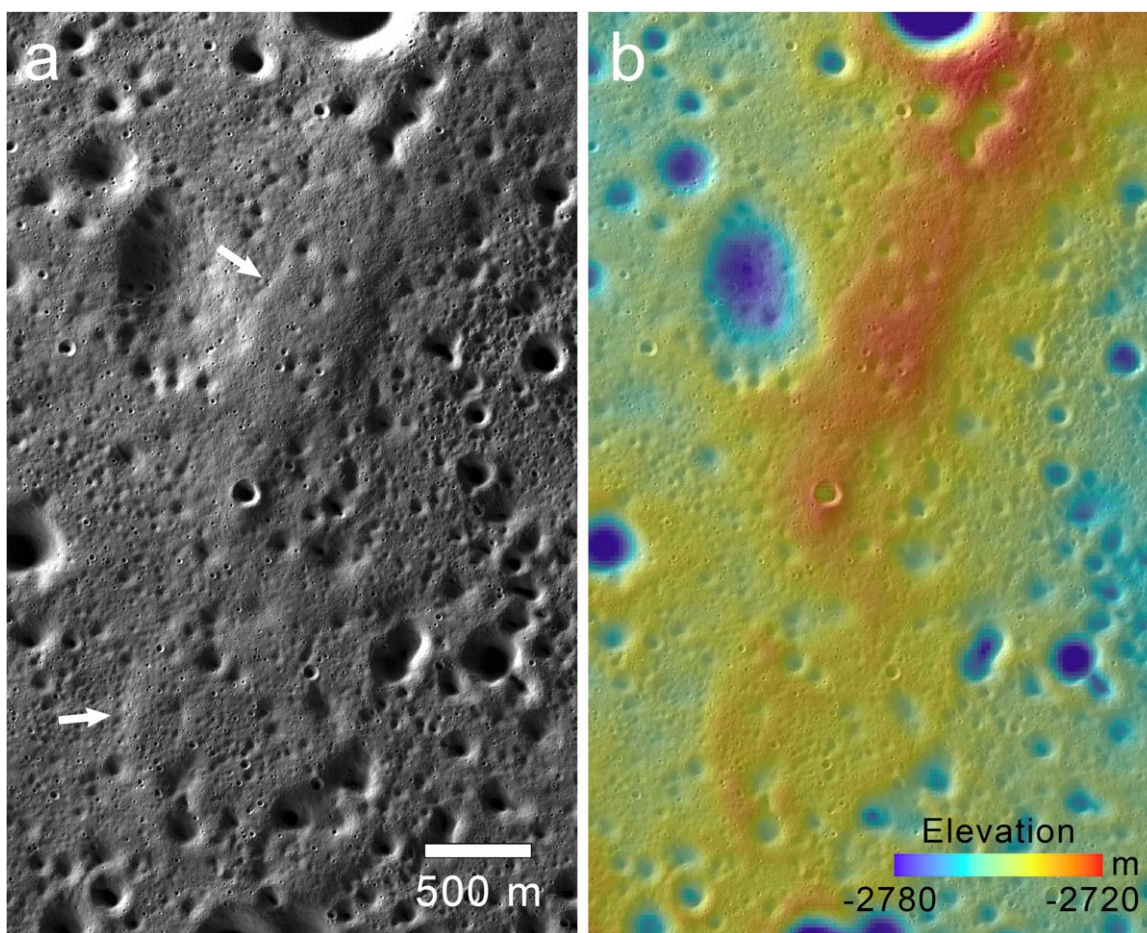


Figure 5. (a) Portion of ShadowCam mosaic, colored with elevation in panel (b), showing a broad ridge dissecting the Lower unit. Portions of the ridge appear bounded by lobate scarps (white arrows). See Figure 3(a) for location.

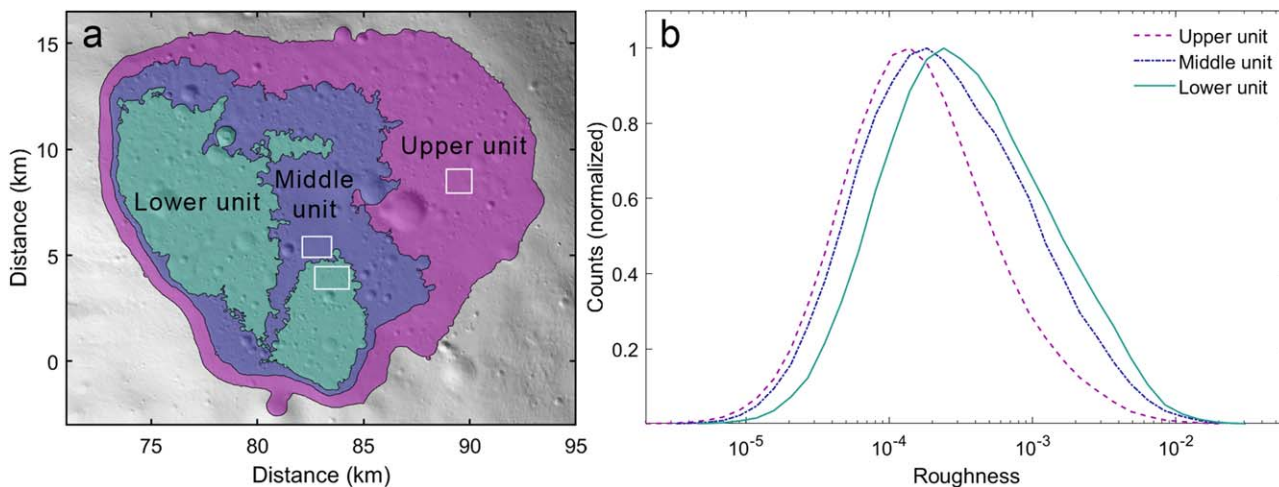


Figure 6. (a) Shaded relief of Faustini floor showing areas used to mask the surface roughness (20 m pixel^{-1} VRM) for the Upper, Middle, and Lower units in Figure 1 to show (b) the distribution of roughness values for these units. Boundaries are based on -2710 and -2740 m elevation contours, with the central mound included in the Middle unit, though it extends above -2710 m. The white boxes are the crater count areas used for Figure 8.

near saturation equilibrium for $D > 30$ m. At smaller diameters ($D < 30$ m) the CSFD departs the saturation curve, and at $D \sim 10$ m it has a similar abundance of craters to the other units. The Middle unit near the central mound has the lowest density of craters, with a CSFD approximating a 100 Ma model production curve (isochron) for craters with $D < 50$ m with a greater abundance of craters at larger sizes, though the CSFD

remains below the 1 Ga isochron. The Lower and Middle unit count areas are in close proximity on either side of the -2740 m elevation contour, demonstrating a distinct difference between the crater populations above and below this elevation, which defines the Lower and Middle units' boundary. The CSFD of the Upper unit is similar to that of the Lower unit at the larger diameters ($D > 60$ m), but the power-law slope is

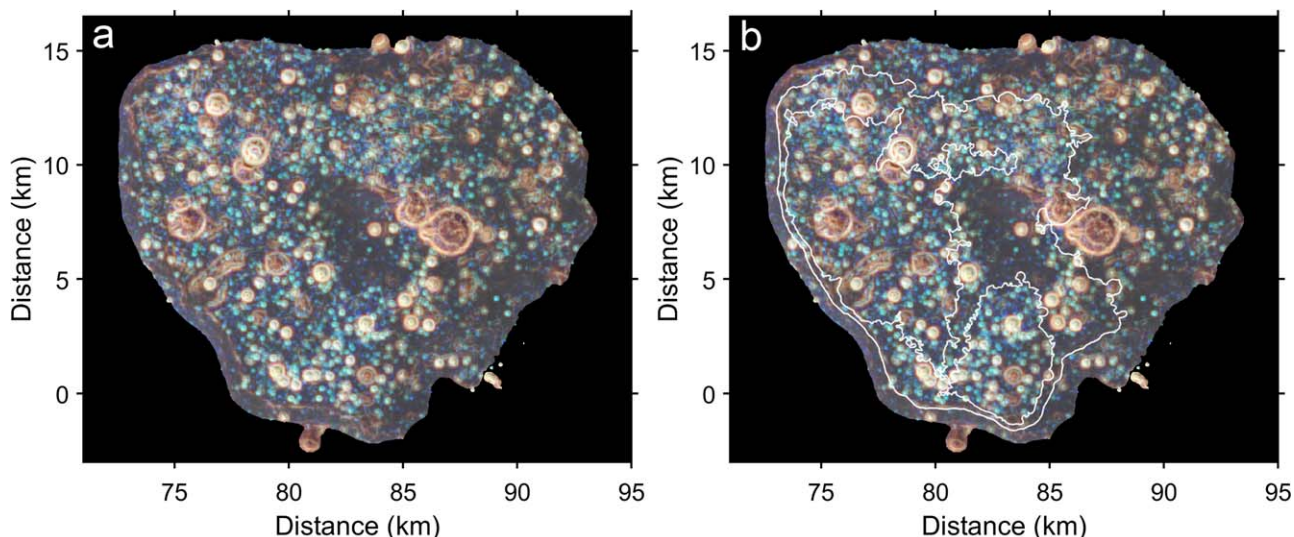


Figure 7. (a) RGB composite of VRM derived from 20, 40, and 80 m pixel⁻¹ DEMs highlighting roughness at different length scales; (b) unit boundaries from Figures 1 and 6 are shown in white for reference.

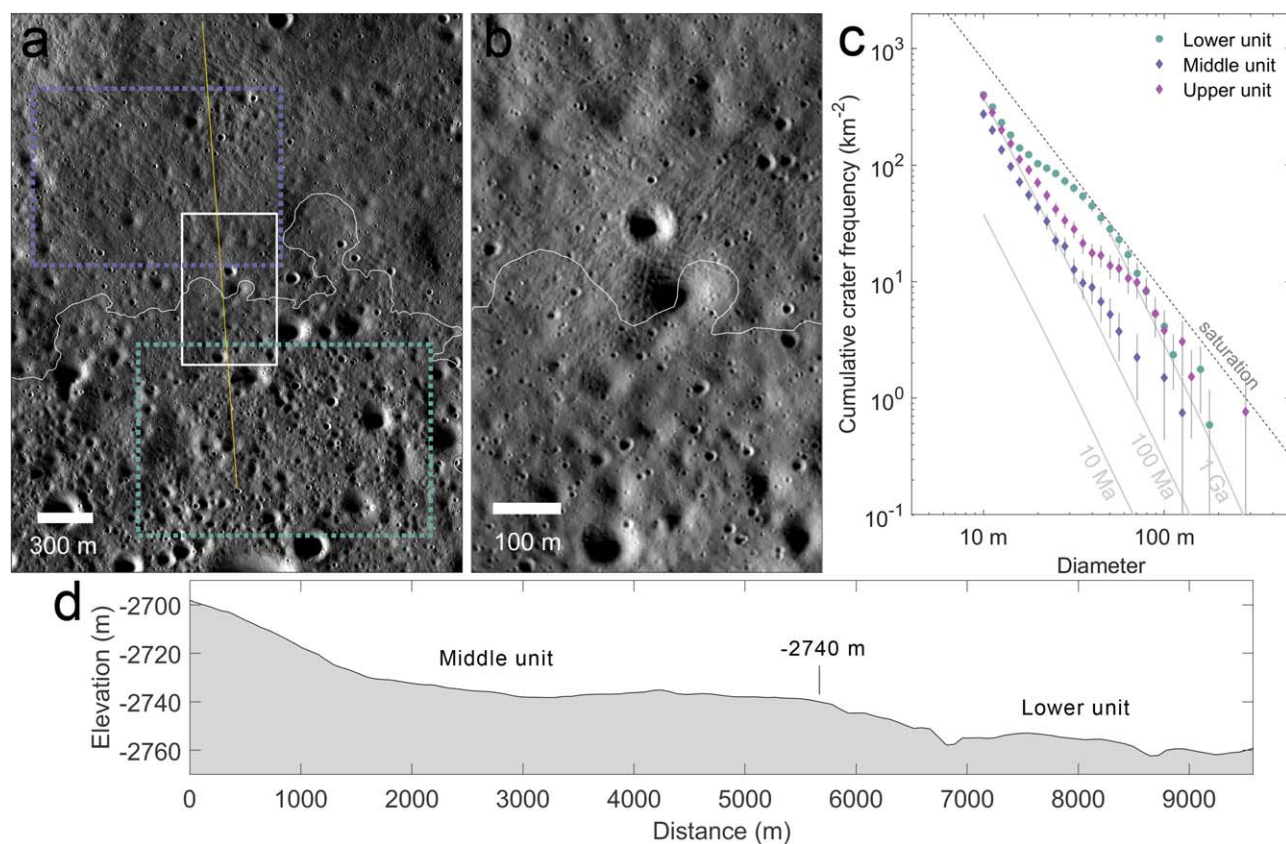


Figure 8. (a) A portion of the ShadowCam mosaic in Figure 1 showing the boundary (thin white line) between the Middle (top) and Lower (bottom) units corresponding to the -2740 m contour. Colored dashed boxes are crater count areas on the Middle and Lower units. The white box is the location of panel (b), showing an enlarged view of the unit boundary with EHT visible on the Middle unit (upper half). (c) CSFDs of the three count areas in panel (a) and Figure 6(a), with absolute model age isochrons (solid) from G. Neukum et al. (2001) and the saturation equilibrium line (dashed) from N. J. Trask (1966). Marker colors reflect the respective colors of the mapped units in Figure 1 and 6 containing the count areas. (d) Elevation profile, with location shown as a yellow line in panel (a). EHT is observed above ~ -2740 m elevation. Count areas correspond to the relatively flat areas of the profile on the Middle and Lower units.

shallower at smaller diameters. All the CSFDs converge to the ~ 100 Ma isochron; however, the diameter range at which they converge to the ~ 100 Ma isochron differs.

Hummocky or wrinkled surface textures, informally referred to as “tree bark” or “elephant hide” texture (EHT), are observed on the Upper and Middle units but absent in the Lower unit

(Figure 8(b)). The formation of EHT is not entirely understood but has been generally assumed to result from the downslope movement of regolith (R. J. Pike 1971; J. Plescia & M. S. Robinson 2010; Z. Xiao et al. 2013; A. Y. Zharkova et al. 2020). EHT has previously been reported in PSRs on surfaces with shallow ($<5^\circ$) slopes in ShadowCam images

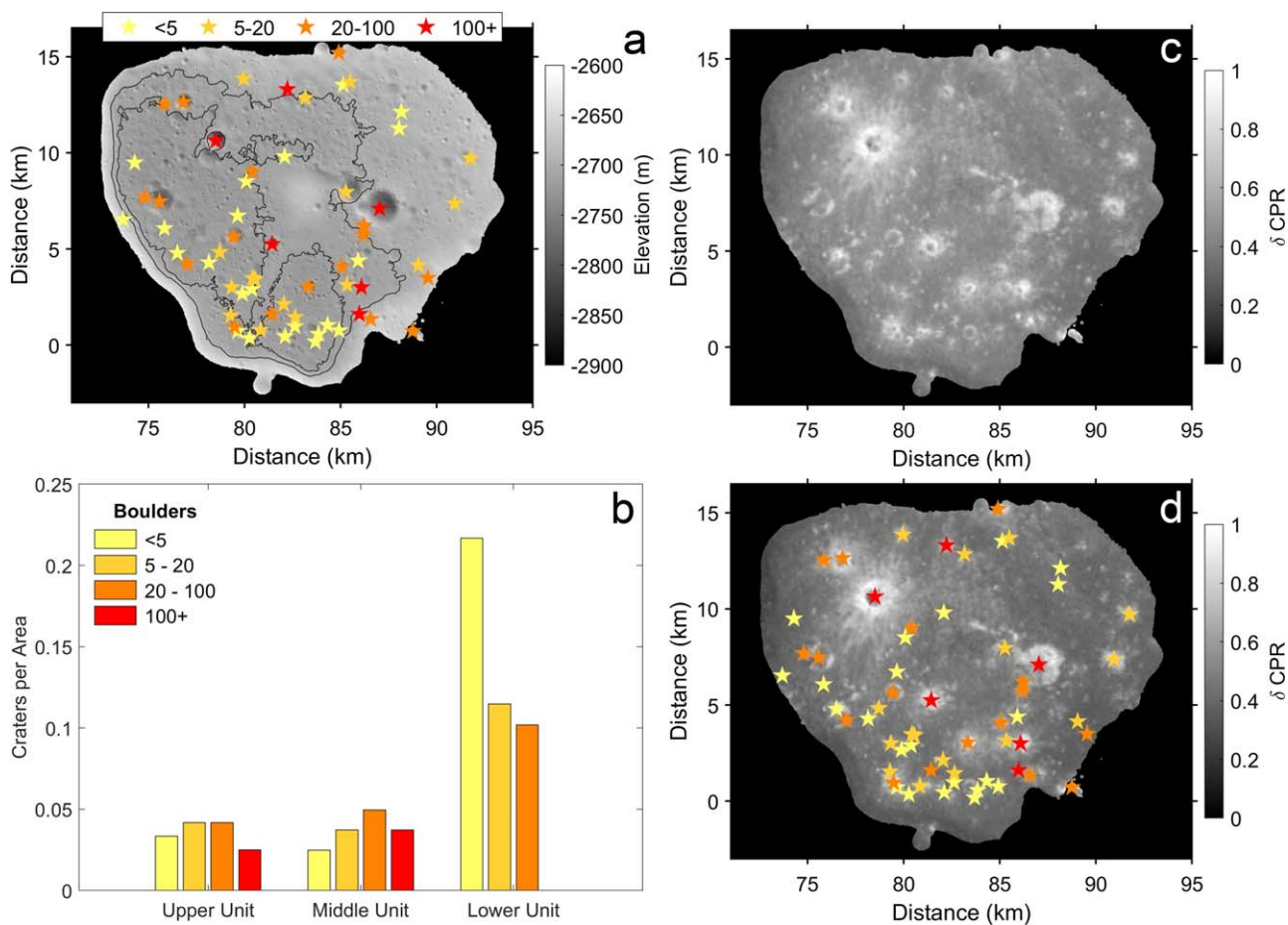


Figure 9. (a) Locations of craters associated with boulders on an elevation map of the Faustini floor with unit boundaries from Figure 1. Craters are categorized by number of boulders from low (<5) to high (>100) and plotted in panel (b) as histograms for each of the units. (c) Mini-RF δ CPR from C. I. Fassett et al. (2024) of the Faustini floor, with crater locations marked in panel (d) showing elevated CPR values where craters with boulders are identified.

(H. Brown et al. 2024), suggesting that EHT can form on regolith with low slopes. While EHT is observed on moderate slopes around degraded craters and the flanks of the central mound in Faustini, it is also observed on relatively flat areas adjacent to the central mound within the Middle unit. However, EHT is absent below the elevation -2740 m on the Lower unit, suggesting that slope does not exclusively drive the formation of EHT (Figure 8(d)).

We observed boulders on the crater floor, which are associated with impact craters in all cases, with the rare exception of a few isolated boulders with no apparent source craters. Boulders are observed within and around craters, with the number of boulders generally corresponding to the preservation state of the craters, where craters with more pronounced rims, and thus likely younger, have a greater number of boulders (e.g., A. T. Basilevsky et al. 2013; R. R. Ghent et al. 2014). Many rimless depressions and pits, presumably highly degraded impact craters, have no resolved boulders. Craters with $D \lesssim 100$ m, regardless of preservation state, lack boulders, suggesting that either a size threshold is required to excavate boulders from depth or the block sizes generated by the smaller craters are no longer resolvable in the ShadowCam images, as the maximum block size diminishes with decreasing crater size (H. J. Moore 1971; H. J. Melosh 1989). Figure 9 shows the locations of the source craters of the boulders observed in ShadowCam imagery, categorized by number of boulders. While the Upper and Middle units have

similar densities of craters with boulders, the Lower unit has a significantly higher density with a higher proportion of smaller craters. This suggests that rocks are more readily excavated from the Lower unit, with smaller, more frequent impacts able to generate craters with boulders. The smaller impacts will generate fewer resolvable boulders and shift the distribution to a higher relative number of craters with a low number of observed boulders. CPR data from LRO’s Miniature Radio-Frequency instrument (Mini-RF; R. L. Kirk et al. 2013; J. T. S. Cahill et al. 2014) show elevated CPR values associated with these craters consistent with the observation that these craters are associated with blocks in ShadowCam images. Figures 9(c) and (d) highlight this with δ CPR data from C. I. Fassett et al. (2024), which show CPR with the effects of incidence angle removed.

We identified four irregularly shaped depressions (Figures 1 and 10), which are quasi-circular to elongated in planform; two are associated with impact craters (Figures 10(e) and (f)). It is unclear whether the craters play a role in the initiation and development of the depressions or are superposed on the depressions and post-date their formation.

4.3. Temperatures

The primary source of scattered and emitted photons within the Faustini PSR is the equator-facing wall, and thus diurnal and seasonal variations in the illumination conditions of the

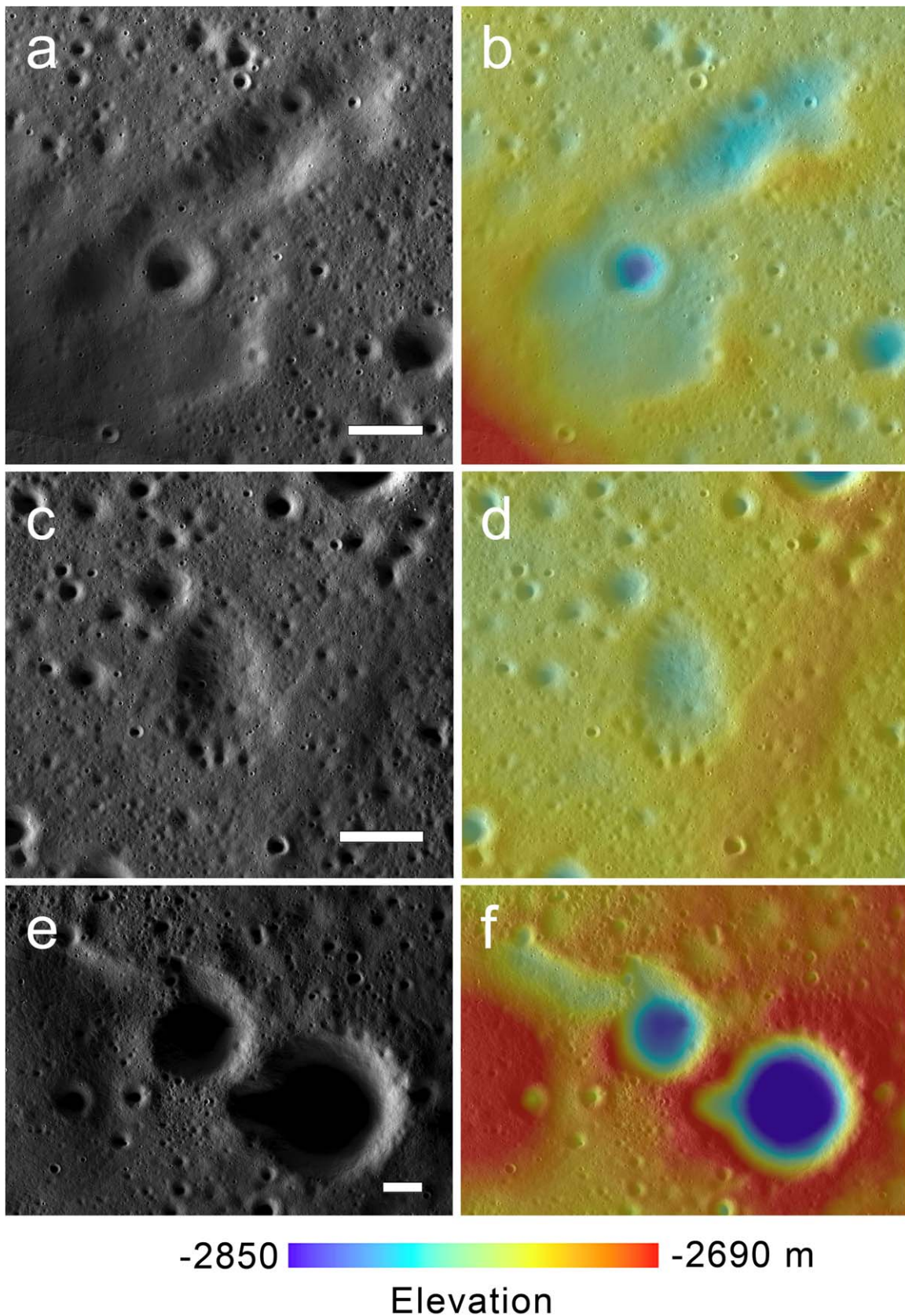


Figure 10. Portions of the ShadowCam mosaic in Figure 1(a) (left column) and colored by elevation (right column) highlighting irregular depressions. (a–b) A quasi-circular depression with an elongated segment in the Lower unit. (c–d) An elliptical, rimless depression in the Lower unit. (e–f) Two deeper depressions, likely remnant impact craters, at the boundary of the Middle and Upper units, with depressions extending beyond the former crater rims. The smaller crater has a more extensive, elongated depression that abuts the central mound on the left side of the figure. White scale bars are 500 m. See Figure 1 for their locations.

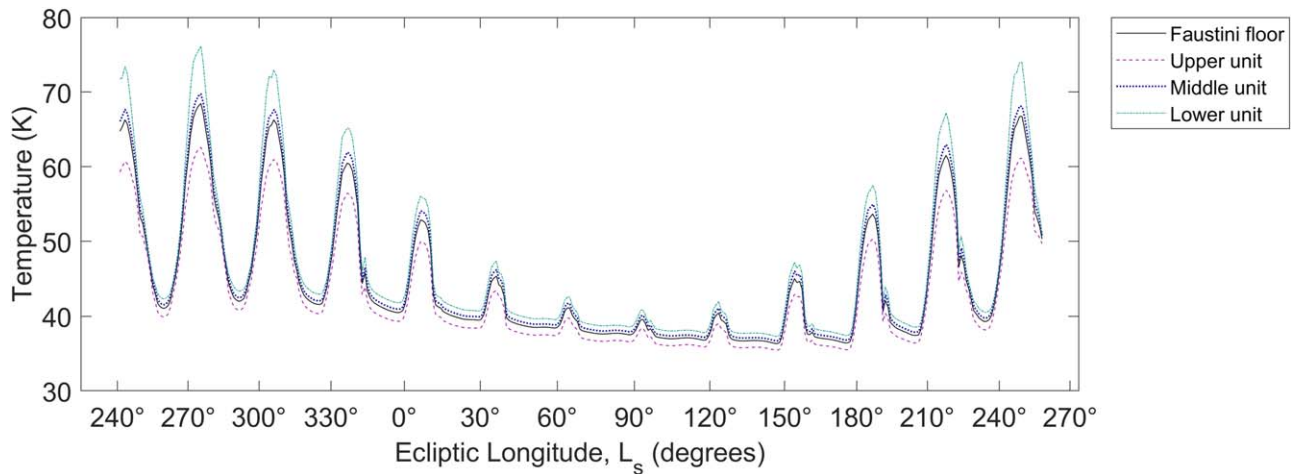


Figure 11. Modeled mean of the Faustini floor surface temperature during the primary KPL0 mission (year 2023), where southern summer solstice is $L_s = 270^\circ$ and southern winter solstice is $L_s = 90^\circ$.

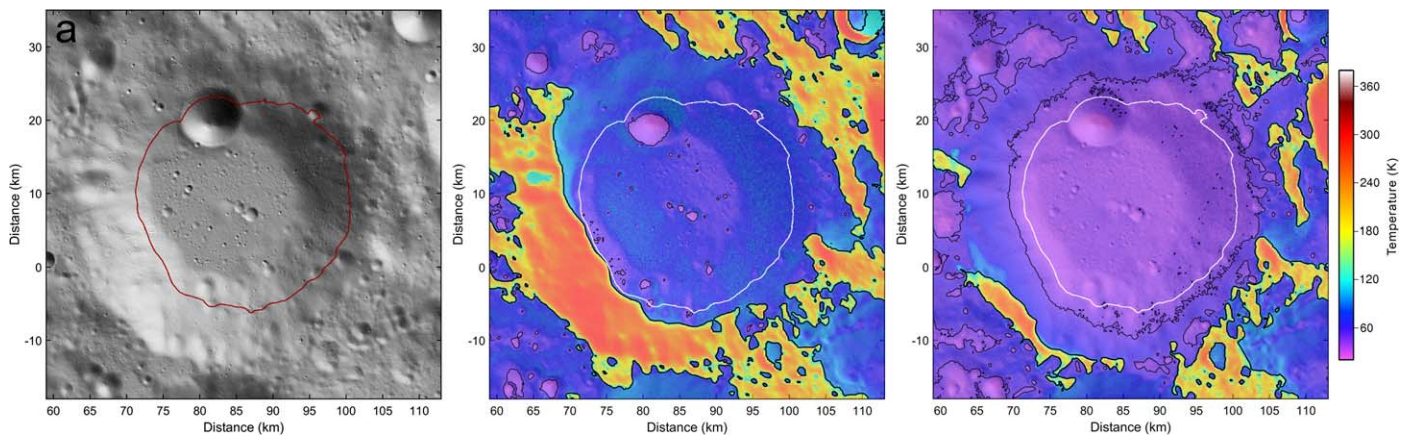


Figure 12. (a) Shaded relief of Faustini crater and colored with model temperatures during (b) the period of peak average temperatures of the crater floor near summer solstice (2024 February 2) and (c) winter solstice (2024 July 27), highlighting differences in the diurnal peak in illumination occurring on the equator-facing wall between the two seasonal extremes. Black temperature contours in panels (b) and (c) are 110 K (thick) and 50 K (thin), representing temperatures at which H_2O and CO_2 sublimation rates become negligible (e.g., N. Schörghofer & J.-P. Williams 2024).

wall modulate the floor temperatures. The temperatures across the floor remain below 110 K. Figure 11 shows an average of the floor temperatures modeled for the duration of the KPL0 primary mission, showing the diurnal temperature variations (synodic period) with the amplitude evolving with the season, defined here by ecliptic longitude (L_s), which provides an angular description of the draconic time of year (0° – 360° ; N. Schörghofer & J.-P. Williams 2020). The start of the primary mission occurred shortly before the southern summer solstice on 2023 January 27 ($L_s = 270^\circ$). Near that date, peak temperatures within the PSR coincided with the maximum extent of illumination of the equator-facing crater wall (Figure 12). Maximum diurnal temperatures are significantly reduced during winter, as only the uppermost portion of the crater wall becomes illuminated, resulting in near-constant, cold temperatures throughout the PSR. Minimum temperatures continue to drift to lower values after the winter solstice, reflecting a long thermal time constant of the PSR consistent with Diviner observations showing warmer temperatures around the autumnal equinox relative to the vernal equinox in the polar regions. Therefore, temperatures are not necessarily identical given different instances of the same illumination from a specific subsolar longitude and latitude.

The warmest temperatures occur in the poleward half of the crater floor due to closer proximity to the equator-facing wall, which can exceed 250 K when illuminated; the pole-facing wall is predominately within the PSR boundary and remains below 95 K throughout the year. Figure 13 shows the asymmetry observed in the maximum and mean temperatures on the floor. ShadowCam image M15308992S in Figure 4 shows this general trend in the radiance from the scattered illumination on the floor when the equator-facing wall is illuminated. Modeled temperatures for the date the image was acquired (Figure 14) highlight the resulting temperature gradient across the floor, with temperatures varying by ~ 30 K between the warmer and colder portions.

The thermal gradient observed on the floor results in a large asymmetry in the water-ice sublimation rate on the floor (>6 orders of magnitude). While sublimation rates remain low enough for the entire floor to be considered a cold trap for water ice, other volatile compounds can have volatility temperatures such that they are predicted to be cold trapped only in the colder portions of the floor. For example, several species detected during the LCROSS impact experiment (A. Colaprete et al. 2010) in the Cabeus PSR and identified in comets (D. Bockelée-Morvan & N. Biver 2017) are

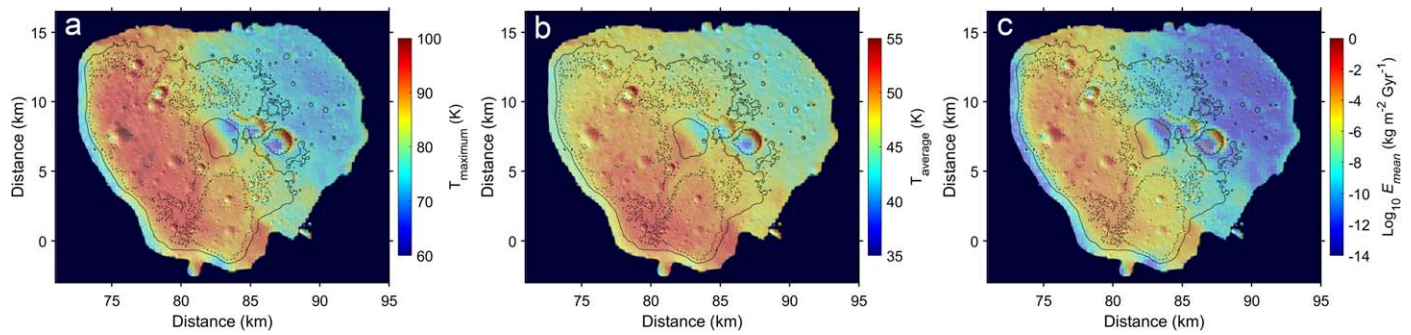


Figure 13. Shaded relief maps of the Faustini floor colored with (a) maximum and (b) average Diviner bolometric temperatures derived from 240 m pixel^{-1} polar stereographic gridded data from J.-P. Williams et al. (2019) and (c) time-averaged sublimation rate of water ice from N. Schörghofer & J.-P. Williams (2020). Elevation contours are -2710 and -2740 m from Figure 3.

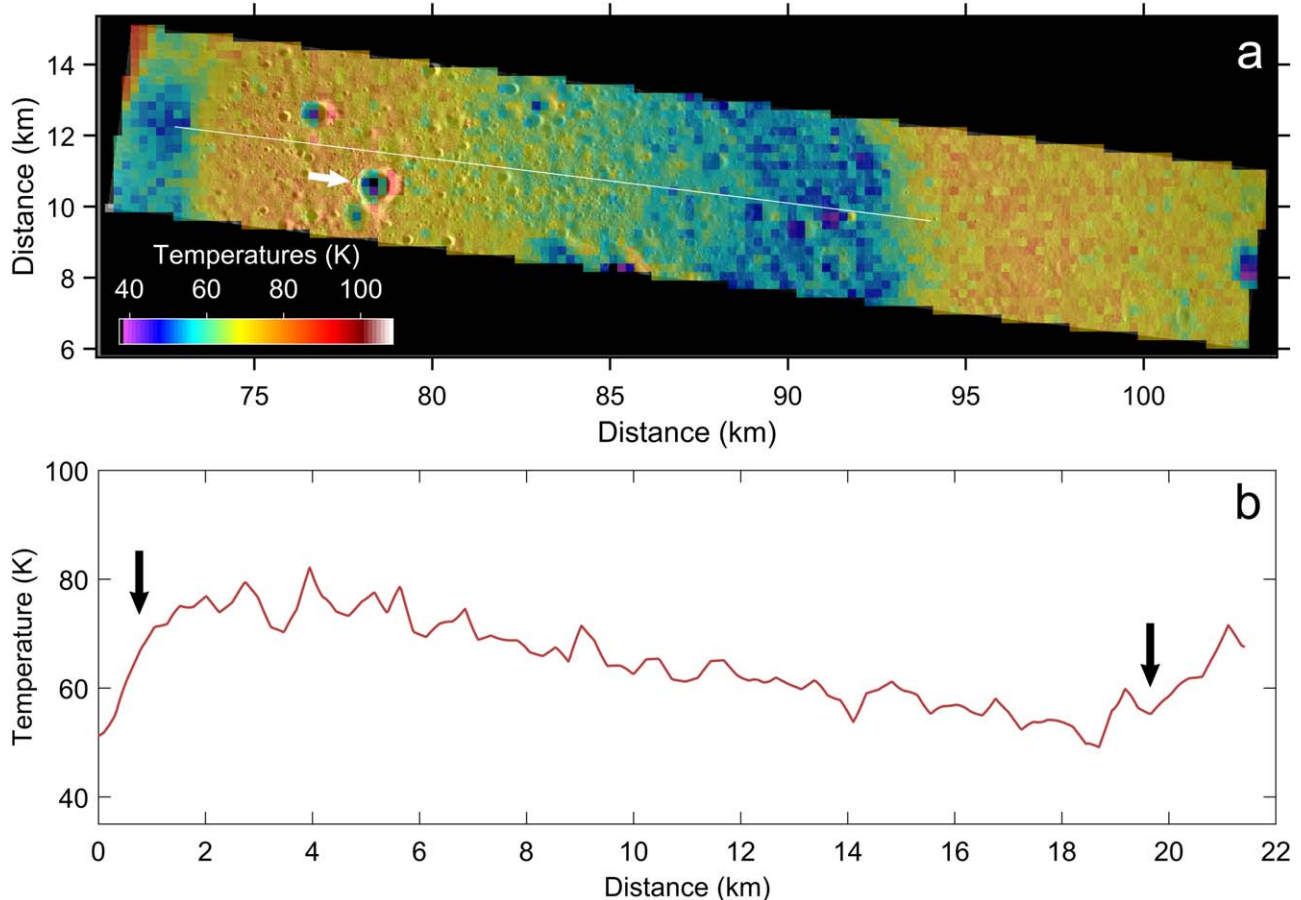


Figure 14. (a) ShadowCam image M15308992S (Figure 4) colored with model temperatures for the date the image was acquired (2023 January 29) and (b) the temperature profile across the floor. Location of image shown in Figure 1(b). The line in panel (a) shows the location of the temperature profile, and white arrow shows the location of an LRC in Figure 16. Black arrows in panel (b) denote the wall/floor contact locations.

predicted to have the potential to be cold trapped to differing extents across the floor (N. Schörghofer & J.-P. Williams 2024; Figure 15(a)). CO_2 is not predicted to be stable at the surface from Diviner temperature data binned at 500 m resolution (N. Schörghofer et al. 2021). However, at smaller scales, colder surfaces that harbor CO_2 could be present due to surface roughness and other small depressions unresolved by Diviner (P. O. Hayne et al. 2021), and if present in the subsurface, CO_2 is predicted to be thermally stable at various depths, primarily due to the attenuation of peak temperatures within the regolith.

CO_2 is predicted to be stable within a few centimeters of the surface in the colder Upper unit and below $\sim 10\text{--}12 \text{ cm}$ depth in the warmer Lower unit (Figure 15(b)).

The coldest temperatures within the Faustini PSR are found in areas that do not have a line of sight to illuminated terrain, thus forming double PSRs (DPSRs). In these areas, illumination requires scattering from multiple surfaces (V. Carruba & A. Coradini 1999; P. O'Brien & S. Byrne 2022). DPSR locations experience extremely low annual minimum temperatures, with Diviner having observed

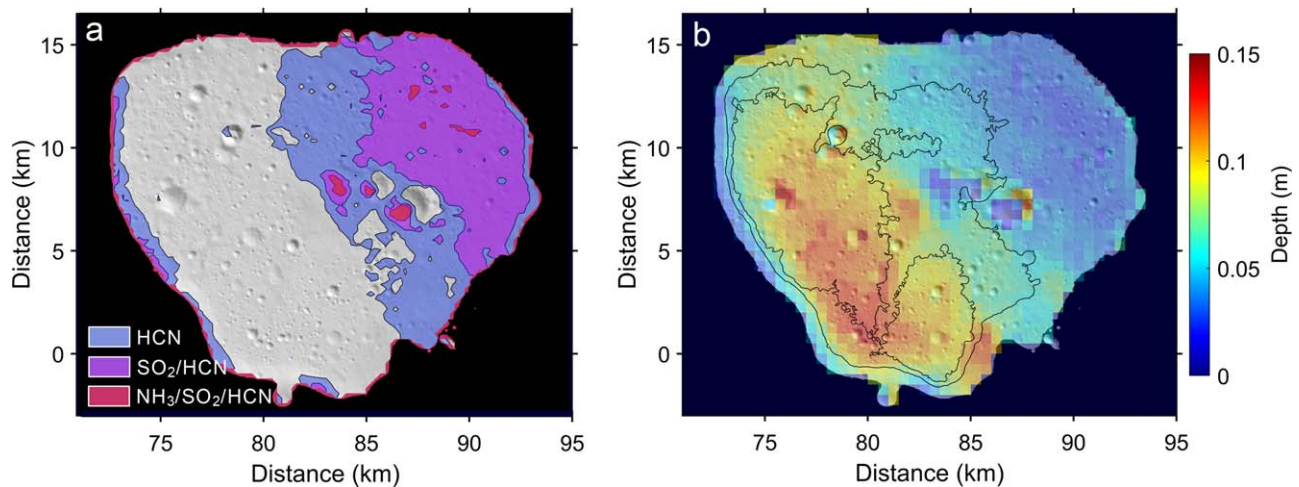


Figure 15. Shaded relief of the Faustini floor showing (a) where the time-average sublimation rates from N. Schörghofer & J.-P. Williams (2024) are below $1 \text{ kg m}^{-2} \text{ Gyr}^{-1}$ for HCN, SO_2 , and NH_3 and (b) the subsurface depth at which the loss rate of $1 \text{ kg m}^{-2} \text{ Gyr}^{-1}$ of solid CO_2 occurs at 500 m resolution from N. Schörghofer et al. (2021). Black lines are unit boundaries from Figure 1.

temperatures $\lesssim 20 \text{ K}$ (K.-M. Aye et al. 2013; D. A. Paige & M. A. Siegler 2016). Such low temperatures allow for the cold trapping of additional supervolatiles (J. A. Zhang & D. A. Paige 2009; M. E. Landis et al. 2022; N. Schörghofer & J.-P. Williams 2024), making these locations favorable for preserving a record of volatile delivery to the poles. Figure 16 highlights a DPSR within a 1.2 km diameter lobate-rim crater (LRC). The LRC possesses an unusual morphology that may suggest that it formed in a target containing subsurface ice (M. S. Robinson et al. 2024). The thermal model predicts that temperatures within the DPSR do not exceed $\sim 55 \text{ K}$, making it a cold trap for several volatile species, including CO_2 .

5. Discussion

The Faustini crater floor exhibits elevation, slope, and surface roughness differences. The Upper unit is predominately sloped toward the pole except around Malinkin crater, where ejecta materials likely contribute to the floor materials. The relatively higher slope and elevation of the Upper unit suggest that a greater deposition of material occurred in this portion of the crater floor, and EHT is observed in some places. Subtle variations in surface roughness and elevation occur within the unit. Detrending the regional slope of the Upper unit reveals broad arcuate ridges partially enclosing shallow depressions (Figure 17). The ridges are smoother, with fewer craters, than their immediate surroundings, suggesting that these localized areas experienced elevated erosion or topographic diffusion rates. The depressions may represent the remnants of two 2 km diameter buried impact craters. Topographic diffusion alone would not explain the near-total erasure of craters of this size, given the estimated age of Faustini of 4.1 Ga (C. I. Fassett & B. J. Thomson 2014; A. R. Tye et al. 2015), and requires the deposition of additional material within this portion of the floor. The density of rocky craters is also much lower in the Upper unit compared with the Lower unit (Figure 9), which would be consistent with a thicker deposit or buildup of regolith on the Upper unit, making it more difficult for impactors to excavate blocky materials from depth (e.g., C. M. Elder et al. 2019; J. Venkatraman et al. 2023).

The Middle unit comprises a relatively flat, transitional region between the Upper and Lower units and contains the

central mound. The central mound and surrounding area have relatively low surface roughness values and comparatively few blocky craters, similar to the Upper unit and ubiquitous EHT.

The Lower unit, by comparison, contains a greater density of craters and higher VRM values. The abundance of blocky craters further suggests that the Lower unit represents a thinner layer of regolith material overlying a rockier subsurface. EHT is absent, and the CSFD shows a greater number of craters at all sizes above $D \sim 20 \text{ m}$ and approaches the saturation equilibrium at larger diameters, similar to the observations of B. W. Denevi et al. (2024).

The deviation of the CSFDs from equilibrium requires the removal of small craters at a rate more rapid than from saturation alone, as craters smaller than $\sim 1\text{--}2 \text{ km}$ should be in saturation equilibrium after 4.1 Gyr. This suggests that craters have been removed by a resurfacing process or event, or material properties have resulted in a reduction in the retention of craters. A volatile-rich substrate could influence the formation and retention of smaller craters (M. E. Banks et al. 2010; A. A. Kokhanov et al. 2015). For example, a latitude trend in roughness on Mars has been attributed to terrain softening, possibly from creep deformation of near-surface ice, or the cyclical deposition and sublimation of frost (S. W. Squyres & M. H. Carr 1986; M. A. Kreslavsky & J. W. Head 2000; M. A. Chamberlain & W. V. Boynton 2007). Crater rims are observed to be broader and rounded, with a paucity of sharp-rimmed, small craters in such areas. The LRC within Faustini (Figure 16) has been suggested to be consistent with subsurface ice (M. S. Robinson et al. 2024), and the irregularly shaped depressions (Figure 10) could be explained by a loss of mass by ice volatilization, resulting in the deflation of the surface materials. Rimless depressions, or hollows, are observed on Mercury and are interpreted to have formed by sublimation of volatile material, though hollows are steep sided, tend to be more irregular in shape and distribution (often appearing in clusters), and likely formed by a recent or ongoing process (D. T. Blewett et al. 2013; R. J. Thomas et al. 2014). The presence of ice within the regolith could alter degradation rates of craters. Additionally, depositional events that deliver volatiles to the PSR could infill craters, and craters in the south polar region are found to have shallower depth-to-diameter ratios on average (A. A. Kokhanov et al. 2015;

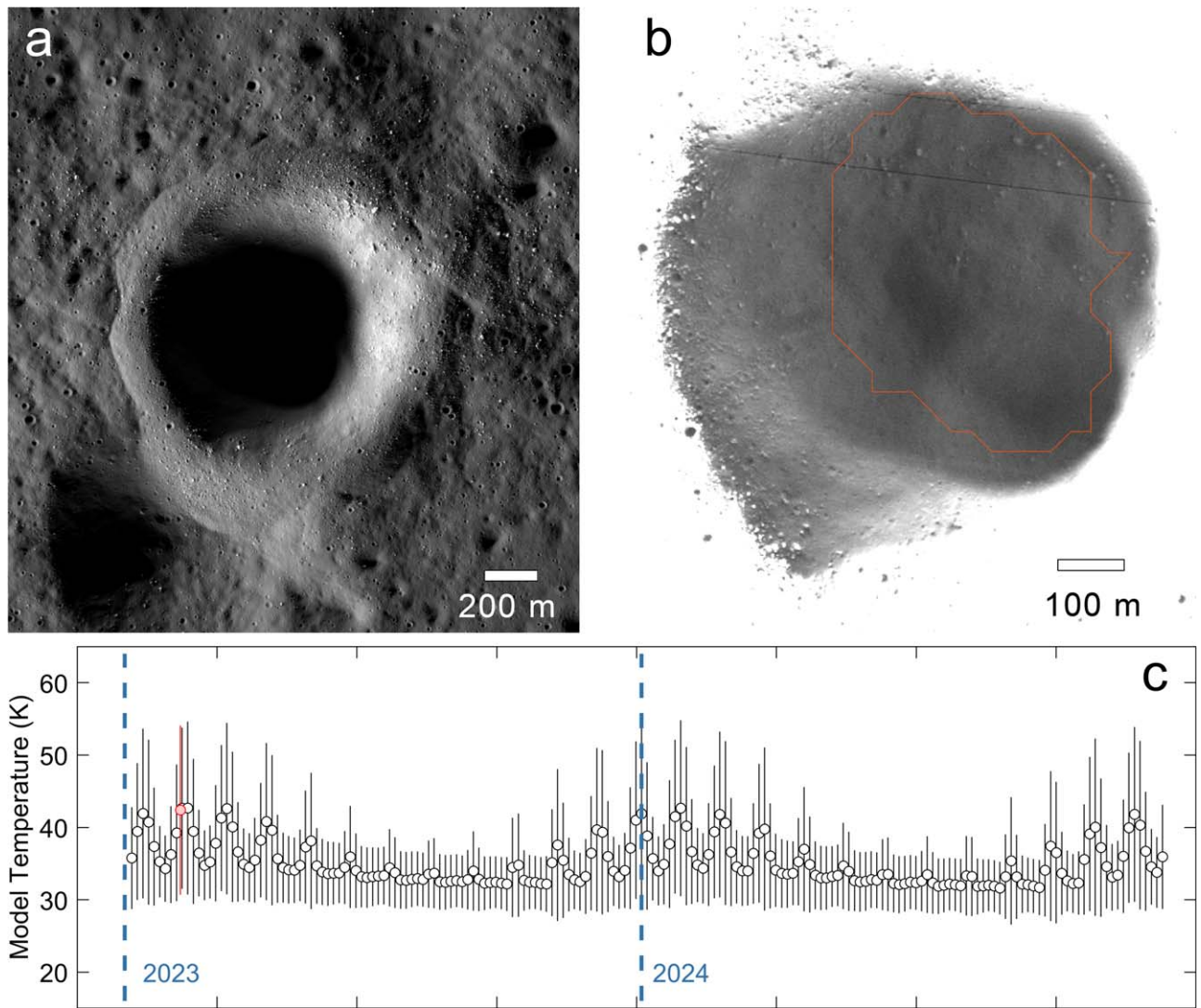


Figure 16. (a) A portion of ShadowCam image M15308992S showing an LRC that contains a DPSR within its interior (M. S. Robinson et al. 2024). (b) The interior of the LRC with the image stretched to highlight the DPSR (orange outline) identified by P. O’Brien & S. Byrne (2022). (c) Model temperatures from within the DPSR polygon in panel (b) for each Earth day for years 2023 and 2024. Markers and error bars are the mean and standard deviation of the temperatures within the polygon. The red point corresponds to the date that image M15308992S was acquired, showing that the image was acquired near an annual temperature maximum. See Figure 14 for the location of the LRC.

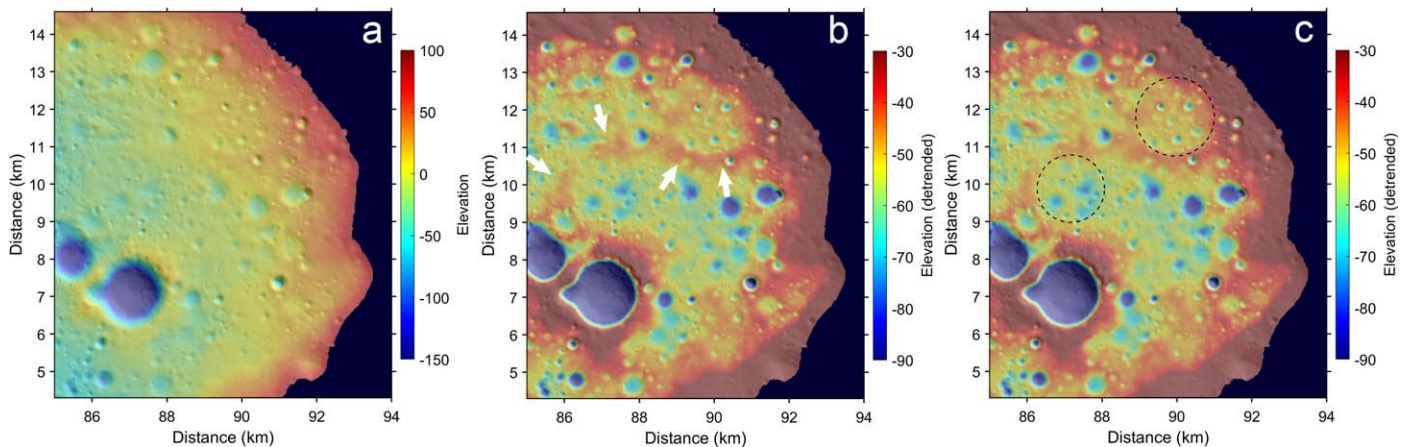


Figure 17. (a) Shaded relief colored by elevation of a portion of the Faustini floor centered on the Upper unit area. (b) Elevation with the local slope removed. White arrows highlight broad, arcuate ridges that are smoother (lower VRM values), and have fewer craters, than their surroundings and circumscribe shallow depressions highlighted with dashed circles in panel (c), which may be the remnants of ~ 2 km diameter impact craters.

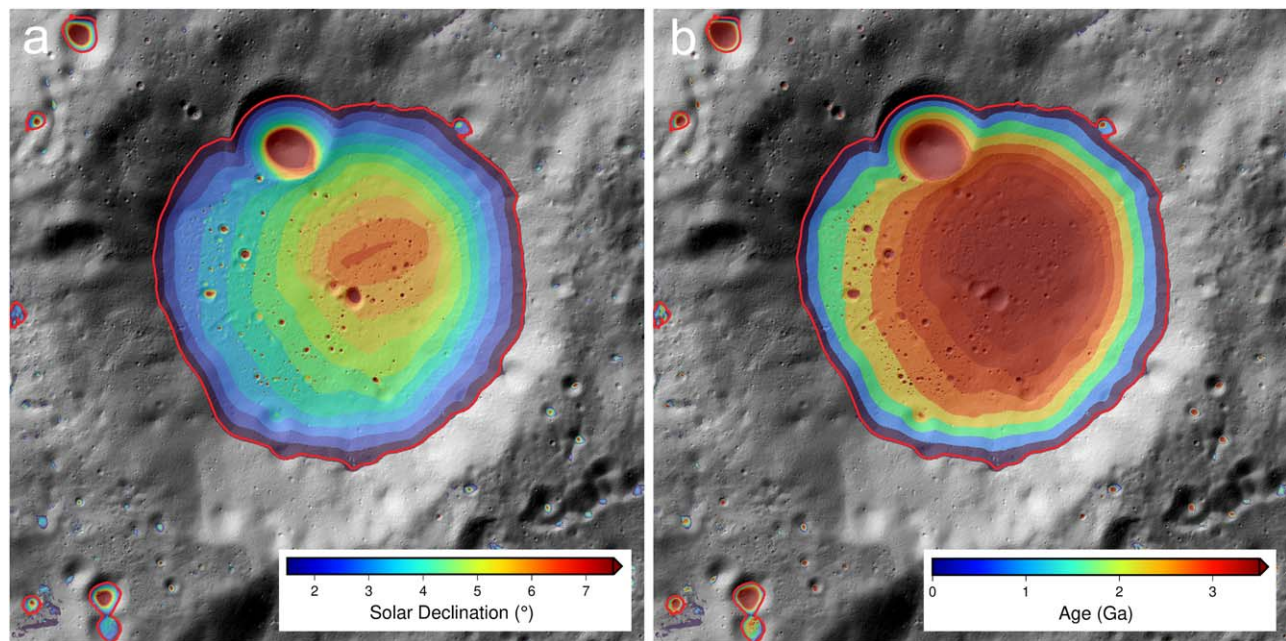


Figure 18. (a) PSR area as a function of solar decl. (N. Schörghofer & R. Rufu 2023). The axial tilt of the Moon has dampened to smaller values over time. Therefore, the map can be interpreted as the relative age of PSR area. (b) Using a model of the Earth–Moon evolution (e.g., R. H. Tyler 2021), the map in panel (a) is converted to a map of maximum PSR age. Here, following N. Schörghofer & R. Rufu (2023), we use the integration of M. Farhat et al. (2022). The red outlines indicate PSRs with areas greater than 1 km^2 .

L. Rubanenko et al. 2019). Such deposition could potentially remove smaller craters. However, a uniform depositional process would fill craters on all units of the Faustini floor and remove craters across all units systematically. The CSFDs of the Upper and Middle units have larger deviations from equilibrium with greater deficits in craters, suggesting inherent differences in the size dependence of crater retention between the units. This difference in retention suggests nonuniform deposition of materials or nonuniform degradation rates between the units.

Alternately to the effect of ice, the greater thicknesses of rock-free regolith in the Upper and Middle units, implied by the differences in blocky crater densities and higher surface elevations, could result in a more rapid removal rate of small craters (Z. Xiao & S. C. Werner 2015). The presence of EHT on the Upper and Middle units, but its absence on the Lower unit, would suggest that lateral transport of regolith materials has been nonuniform and thus could explain a difference in crater retention rates between the units. The presence of volatiles may or may not play a role. Sublimation rates between the units differ considerably (Figures 13 and 15), due to the mean poleward temperature gradient across the floor. The cold trapping potential for various volatile species varies across the floor and could alter regolith properties. Additionally, the Upper unit has been a PSR for a longer portion of lunar history. As the Moon’s obliquity relative to the ecliptic plane has evolved from a higher value to the current $\sim 1^\circ 54'$, the size of the Faustini PSR has increased, and as a result, the Lower unit has been a cold trap for a shorter period (Figure 18).

Differences in mechanisms and rates of mass wasting on the crater walls could also contribute to variations in surface properties across the floor. Temperatures of the crater walls vary substantially. The equator-facing wall is illuminated nearly down to the floor around summer solstice, and surface temperatures can exceed 250 K. The poleward-facing wall, by comparison, is nearly entirely within the PSR, and temperatures

remain below $\sim 100 \text{ K}$; thus, the wall is a cold trap for water ice. This temperature discrepancy may result in differences in competencies of wall materials and downslope erosion of materials onto the floor between the two halves of the crater, resulting in thicker deposits on the colder side of the floor. Alternately, the formation of nearby Amundsen crater could have deposited ejecta material on the colder side of Faustini, resulting in a thicker blanket of material on that half of the floor and surrounding wall, resulting in a material property asymmetry (D. E. Wilhelms et al. 1979).

We observe textural differences between the cold and warm walls of the crater (Figure 19), and the VRM values are elevated on the cold wall owing to a hummocky texture often associated with exposed boulders. The warm wall that experiences periods of direct illumination has lower VRM values by comparison. The exception is an area of elevated VRM values aligned with the wall slope extending from beyond the crater rim to the crater floor, suggesting that a mass wasting event may have occurred. Such an event could have been triggered by debris impacting the rim during the formation of Shackleton. Another portion of the wall with elevated roughness values occurs on the opposite side of the crater. Pitting on the wall in this location is observed in ShadowCam images (Figure 19(c)). The radial alignment of these two locations with Shackleton, as well as the pitted texture of the northern interior wall, suggests that debris ejected from Shackleton may have struck the wall. Alignments of roughness with Shackleton are not observed on the floor, thus requiring a shallow launch angle of material (no greater than $\sim 4.5^\circ$) to only strike the exterior south rim of Faustini crater and northern interior wall, but not the floor. These occurrences suggest that materials from Shackleton will be found within the center of the Artemis III candidate landing region named “Faustini Rim A.”

Additional alignments of roughness are observed across Faustini that are not radial to Shackleton crater. Two sets of ray segments are identified (Figure 19), and Tycho and Jackson craters are candidate source craters based on their orientations

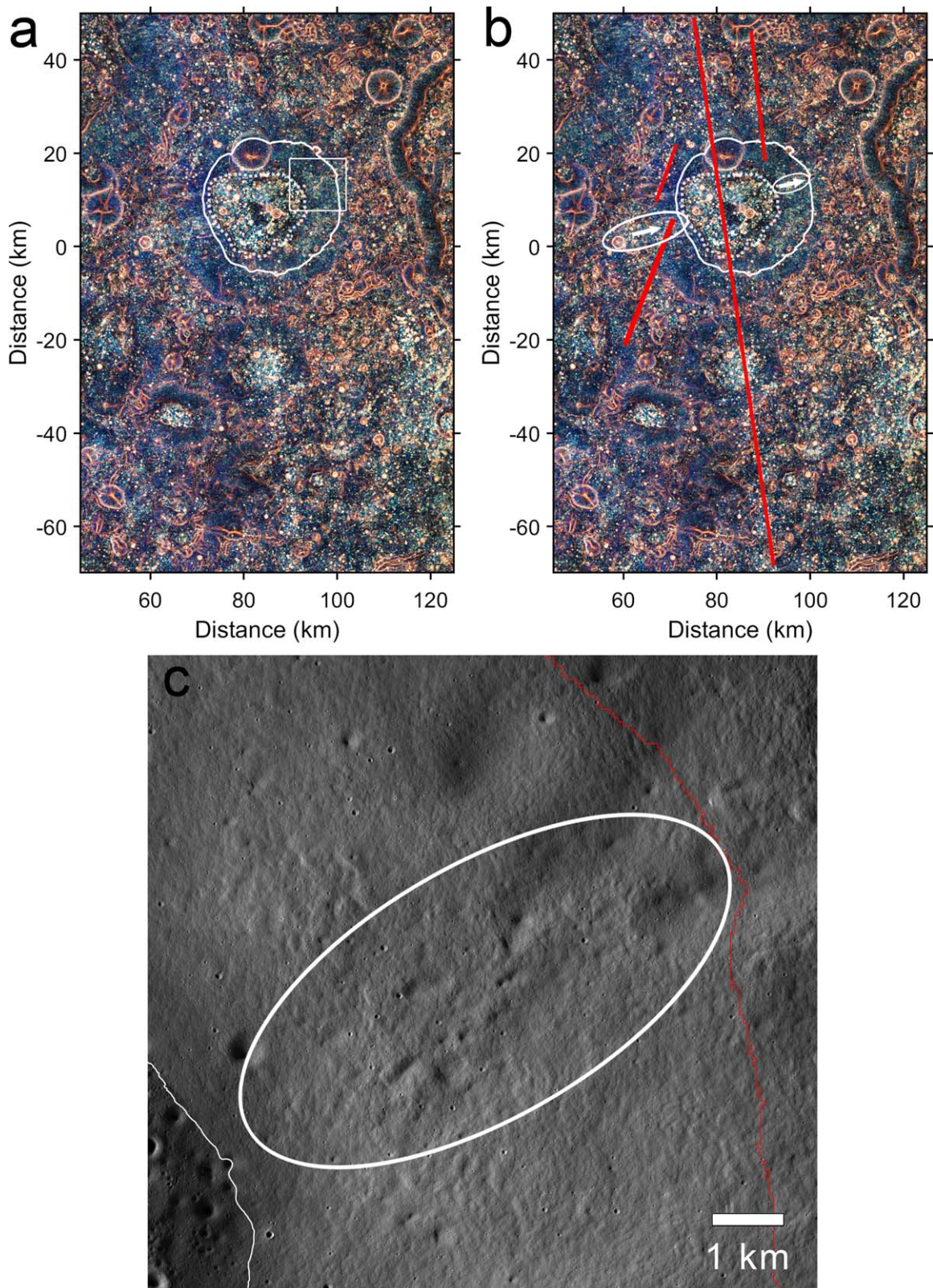


Figure 19. (a) Polar stereographic map of surface roughness (RGB composite of VRM at 20, 40, and 80 m pixel⁻¹) of the region around Faustini crater. The Faustini PSR is outlined by a white solid line, and the Faustini floor is outlined by a white dotted line. Roughness is generally elevated on the cold wall within the PSR (right side) relative to the warm equator-facing side (left side). Linear zones of elevated roughness with two distinct orientations are highlighted with red lines in panel (b) and are likely ray segments from Tycho and Jackson craters given their orientations. Two other zones of elevated roughness are outlined by white ellipses and may result from ejected debris originating from Shackleton. Arrows illustrate the direction of delivery. (c) Portion of ShadowCam mosaic showing part of the poleward-facing wall. The red line is the PSR boundary, and the thin white line is the wall-floor contact. The white ellipse highlights a region of elevated roughness with possible degraded secondary craters from Shackleton. The location of the image is shown as the white box in panel (a).

(B. W. Denevi et al. 2023; M. K. Barker et al. 2023; E. G. Rivera-Valentín et al. 2024). These factors may also contribute to heterogeneities in the observed distribution of craters and surface roughness in and around the Faustini PSR.

No definitive albedo contrasts attributable to the presence of surface volatiles are observed in ShadowCam images of the Faustini PSR despite temperatures conducive to cold trapping of water ice and other volatiles at the surface and spectral evidence for the presence of surface exposed ice (P. O. Hayne et al. 2015; S. Li et al. 2018). The asymmetry in surface roughness and crater degradation does imply an asymmetry in the rate of regolith migration and possibly topographic diffusion rates that may relate to differences in temperature and volatile cold trapping and retention. Previous laboratory experiments suggest that high fractions of water ice (>20–30 wt%) are required to significantly elevate the surface albedo to have an observable contrast in optical images such as ShadowCam's (Z. Yoldi et al. 2015; N. De Castro & S. Li 2024). Therefore, the fraction of water mixed with regolith must be below fractional 20–30 wt% or is beneath the surface. Landforms such as the LRC and irregular-shaped depressions could result from the presence of volatiles in the regolith. Elevated CPR in Mini-RF, however, appears to correspond to craters associated with visible blocks in ShadowCam images and does not definitively indicate the presence of ices.

6. Conclusions

Three distinct units of the floor of Faustini are identified from mapping the topography, slopes, and surface roughness. We interpret the Upper and Middle units to represent thicker deposits on the floor and are smoother with fewer impact craters than the Lower unit. The Lower unit is separated by a low ridge that is interpreted to be a ~4 km long lobate scarp. An asymmetry in surface properties such as crater retention rates and surface roughness and textures suggests that regolith mobility and topographic diffusion rates may vary between the units. Temperatures, and thus volatile cold trapping, generally correspond to the observed variation in surface properties. Therefore, variation in the presence or concentrations of volatiles may explain the asymmetry in surface properties. However, volatiles are not necessary to explain the differences, and the correlation with temperature could be coincidental. Material projected onto a portion of Faustini from Amundsen could also provide an explanation for differences in material properties across the Faustini PSR.

Acknowledgments


We thank the two anonymous reviewers for their expeditious and helpful reviews. This work was funded in part by the NASA Lunar Reconnaissance Orbiter project, under contract with NASA, and the Korea Pathfinder Lunar Orbiter (KPLO) Participating Scientist Program (PSP) under award No. 80NSSC21K0711.

ORCID iDs

Jean-Pierre Williams  <https://orcid.org/0000-0003-4163-2760>

Prasun Mahanti  <https://orcid.org/0000-0003-0805-8074>

Mark S. Robinson  <https://orcid.org/0000-0001-9964-2932>

Robert V. Wagner  <https://orcid.org/0000-0001-5999-0721>

Marley Chertok  <https://orcid.org/0000-0001-9651-6746>

Norbert Schörghofer  <https://orcid.org/0000-0002-5821-4066>

Erwan Mazarico  <https://orcid.org/0000-0003-3456-427X>

Brett W. Denevi  <https://orcid.org/0000-0001-7837-6663>

Shuai Li  <https://orcid.org/0000-0002-9885-0809>

David A. Paige  <https://orcid.org/0009-0001-6122-9904>

References

- Arnold, J. R. 1979, *JGR*, **84**, 5659
- Aye, K.-M., Paige, D. A., Foote, M. C., Greenhagen, B. T., & Siegler, M. A. 2013, *LPSC*, **44**, 3016
- Banks, M. E., Byrne, S., Galla, K., et al. 2010, *JGRE*, **115**, E08006
- Barker, M. K., Mazarico, E., Neumann, G. A., et al. 2023, *PSJ*, **4**, 183
- Basilevsky, A. T., Head, J. W., & Horz, F. 2013, *P&SS*, **89**, 118
- Bickel, V. T., Moseley, B., Hauber, E., et al. 2022, *GeoRL*, **49**, e99530
- Bickel, V. T., Moseley, B., Lopez-Francos, I., & Shirley, M. 2021, *NatCo*, **12**, 5607
- Blewett, D. T., Vaughan, W. M., Xiao, Z., et al. 2013, *JGRE*, **118**, 1013
- Bockelée-Morvan, D., & Biver, N. 2017, *RSPTA*, **375**, 20160252
- Brown, H. M., Boyd, A. K., Denevi, B. W., et al. 2022, *Icar*, **377**, 114874
- Brown, H., Wagner, R., & Robinson, M. S. 2024, *LPSC*, **55**, 2589
- Bussey, D. B. J., Lucey, P. G., Steutel, D., et al. 2003, *GeoRL*, **30**, 1278
- Bussey, D. B. J., Spudis, P. D., & Robinson, M. S. 1999, *GeoRL*, **26**, 1187
- Cahill, J. T. S., Thomson, B. J., Patterson, G. W., et al. 2014, *Icar*, **243**, 173
- Campbell, B. A. 2012, *JGRE*, **117**, E06008
- Campbell, D. B., Campbell, B. A., Carter, L. M., Margot, J.-L., & Stacy, N. J. S. 2006, *Natur*, **443**, 835
- Carruba, V., & Coradini, A. 1999, *Icar*, **142**, 402
- Chamberlain, M. A., & Boynton, W. V. 2007, *JGRE*, **112**, E06009
- Cisneros, E., Awumah, A., Brown, H., et al. 2017, *LPSC*, **48**, 2469
- Clark, R. N. 2009, *Sci*, **326**, 562
- Colaprete, A., Elphic, R. C., Heldmann, J., & Ennico, K. 2012, *SSRv*, **167**, 3
- Colaprete, A., Schultz, P., Heldmann, J., et al. 2010, *Sci*, **330**, 463
- De Castro, N., & Li, S. 2024, *LPSC*, **55**, 2283
- Denevi, B. W., Fassett, C. I., Robinson, M. S., et al. 2024, *LPSC*, **55**, 1491
- Denevi, B. W., Rivera-Valentín, E. G., Fassett, C., et al. 2023, in *Artemis III Candidate Landing Regions Workshop*, 2034
- Deutsch, A. N., Heldmann, J. L., Colaprete, A., Cannon, K. M., & Elphic, R. C. 2021, *PSJ*, **2**, 213
- Eke, V. R., Teodoro, L. F. A., & Elphic, R. C. 2009, *Icar*, **200**, 12
- Elder, C. M., Douglass, B., Ghent, R. R., et al. 2019, *JGRE*, **124**, 3373
- Elphic, R. C., Eke, V. R., Teodoro, L. F. A., Lawrence, D. J., & Bussey, D. B. J. 2007, *GeoRL*, **34**, L13204
- Fa, W., & Eke, V. R. 2018, *JGRE*, **123**, 2119
- Farhat, M., Auclair-Desrotour, P., Boué, G., & Laskar, J. 2022, *A&A*, **665**, L1
- Fassett, C. I., Bramson, A. M., Cahill, J. T. S., et al. 2024, *PSJ*, **5**, 4
- Fassett, C. I., & Thomson, B. J. 2014, *JGRE*, **119**, 2255
- Feldman, W. C., Lawrence, D. J., Elphic, R. C., et al. 2000, *JGR*, **105**, 4175
- Feldman, W. C., Maurice, S., Binder, A. B., et al. 1998, *Sci*, **281**, 1496
- Feldman, W. C., Maurice, S., Lawrence, D. J., et al. 2001, *JGR*, **106**, 23231
- Fisher, E. A., Lucey, P. G., Lemelin, M., et al. 2017, *Icar*, **292**, 74
- Frankel, K. L., & Dolan, J. F. 2007, *JGRF*, **112**, F02025
- Ghent, R. R., Hayne, P. O., Bandfield, J. L., et al. 2014, *Geo*, **42**, 1059
- Gladstone, G. R., Hurley, D. M., Retherford, K. D., et al. 2010, *Sci*, **330**, 472
- Gladstone, G. R., Retherford, K. D., Egan, A. F., et al. 2012, *JGRE*, **117**, 2011JE003913
- Hayne, P. O., Aharonson, O., & Schörghofer, N. 2021, *NatAs*, **5**, 169
- Hayne, P. O., Greenhagen, B. T., Foote, M. C., et al. 2010, *Sci*, **330**, 477
- Hayne, P. O., Hendrix, A., Sefton-Nash, E., et al. 2015, *Icar*, **255**, 58
- Hendrix, A. R., Retherford, K. D., Randall Gladstone, G., et al. 2012, *JGRE*, **117**, E12001
- Heyer, T., Iqbal, W., Oetting, A., et al. 2023, *P&SS*, **231**, 105687
- Hobson, R. D. 1972, in *Spatial Analysis in Geomorphology*, ed. R. J. Chorley (New York: Harper and Row), 221
- Honniball, C. I., Lucey, P. G., Ferrari-Wong, C. M., et al. 2020, *JGRE*, **125**, e2020JE006484
- Honniball, C. I., Lucey, P. G., Li, S., et al. 2021, *NatAs*, **5**, 121
- Humm, D. C., Kinczyk, M. J., Brylow, S. M., et al. 2023, *JASS*, **40**, 173
- Hurley, D. M., Gladstone, G. R., Stern, S. A., et al. 2012, *JGRE*, **117**, E00H07
- Ingersoll, A. P., Svitek, T., & Murray, B. C. 1992, *Icar*, **100**, 40
- Jeon, M.-J., Cho, Y.-H., Kim, E. K., et al. 2024, *JASS*, **41**, 43
- Kirk, R. L., Becker, T. L., Shinaman, J., et al. 2013, *LPSC*, **44**, 2920
- Kloos, J. L., Moores, J. E., Sangha, J., Nguyen, T. G., & Schörghofer, N. 2019, *JGRE*, **124**, 1935

- Kneissl, T., van Gasselt, S., & Neukum, G. 2011, *P&SS*, **59**, 1243
- Koeber, S. D., Robinson, M. S., & Speyerer, E. J. 2014, *LPSC*, **45**, 2811
- Kokhanov, A. A., Kreslavsky, M. A., & Karachevtseva, I. P. 2015, *SoSyR*, **49**, 295
- Kreslavsky, M. A., & Head, J. W. 2000, *JGR*, **105**, 26695
- Landis, M. E., Hayne, P. O., Williams, J.-P., Greenhagen, B. T., & Paige, D. A. 2022, *PSJ*, **3**, 39
- Lawrence, D. J. 2017, *JGRE*, **122**, 21
- Li, S., Lucey, P. G., Milliken, R. E., et al. 2018, *PNAS*, **115**, 8907
- Lucey, P. G., Petro, N., Hurley, D. M., et al. 2022, *ChEG*, **82**, 125858
- Luchsinger, K. M., Chanover, N. J., & Strycker, P. D. 2021, *Icar*, **354**, 114089
- Magaña, L. O., Prem, P., Deutsch, A. N., et al. 2024, *PSJ*, **5**, 30
- Margot, J. L., Campbell, D. B., Jurgens, R. F., & Slade, M. A. 1999, *Sci*, **284**, 1658
- Mazarico, E., Neumann, G. A., Smith, D. E., Zuber, M. T., & Torrence, M. H. 2011, *Icar*, **211**, 1066
- Mazarico, E., Neumann, G. A., Barker, M. I. K., et al. 2018, *P&SS*, **162**, 2
- Melosh, H. J. 1989, *Impact Cratering: A Geologic Process* (New York: Oxford Univ. Press)
- Mishra, A., & Senthil Kumar, P. 2022, *GeoRL*, **49**, e98505
- Mitrofanov, I. G., Sanin, A. B., Boynton, W. V., et al. 2010, *Sci*, **330**, 483
- Moon, S., Paige, D. A., Siegler, M. A., & Russell, P. S. 2021, *GeoRL*, **48**, e90780
- Moore, H. J. 1971, *NASA SP-232, Analysis of Apollo 10 Photography and Visual Observations*, 26
- Moseley, B., Bickel, V. T., Lopez-Francos, I., & amd Rana, L. 2021, *IEEE/CVF Conf. on Computer Vision and Pattern Recognition (CVPR)* (Piscataway, NJ: IEEE), 6317
- NASA-Press 2022, *NASA Identifies Candidate Regions for Landing Next Americans on Moon*, <https://www.nasa.gov/news-release/nasa-identifies-candidate-regions-for-landing-next-americans-on-moon/>
- Neukum, G., Ivanov, B. A., & Hartmann, W. K. 2001, *Chronology and Evolution of Mars. Series: Space Sciences Ser. of ISSI, Vol. 12* (Dordrecht: Springer), 55
- Nozette, S., Spudis, P. D., Robinson, M. S., et al. 2001, *JGR*, **106**, 23253
- O'Brien, P., & Byrne, S. 2022, *PSJ*, **3**, 258
- Paige, D. A., Foote, M. C., Greenhagen, B. T., et al. 2010a, *SSRv*, **150**, 125
- Paige, D. A., & Siegler, M. A. 2016, *LPSC*, **47**, 2753
- Paige, D. A., Siegler, M. A., Zhang, J. A., et al. 2010b, *Sci*, **330**, 479
- Paige, D. A., Wood, S. E., & Vasavada, A. R. 1992, *Sci*, **258**, 643
- Patterson, G. W., Stickle, A. M., Turner, F. S., et al. 2017, *Icar*, **283**, 2
- Pieters, C. M., Goswami, J. N., Clark, R. N., et al. 2009, *Sci*, **326**, 568
- Pike, R. J. 1971, *NASA Spec. Publ., NASA-SP-232, Analysis of Apollo 10 Photography and Visual Observations*, 14
- Pizer, S. M., Amburn, E. P., Austin, J. D., et al. 1987, *CVGIP*, **39**, 355
- Plescia, J., & Robinson, M. S. 2010, *European Planetary Science Congress*, 731
- Qiao, L., Ling, Z., Head, J. W., Ivanov, M. A., & Liu, B. 2019, *E&SS*, **6**, 467
- Riley, S. J., DeGloria, S. D., & Elliot, R. 1999, *Intermountain Journal of Sciences*, **5**, 23
- Rivera-Valentín, E. G., Fassett, C. I., Denevi, B. W., et al. 2024, *PSJ*, **5**, 94
- Robinson, M. S., Brylow, S. M., Caplinger, M. A., et al. 2023, *JASS*, **40**, 149
- Robinson, M. S., Brylow, S. M., Tschimmel, M., et al. 2010, *SSRv*, **150**, 81
- Robinson, M. S., Mahanti, P., Bussey, D. B. J., et al. 2024, *LPSC*, **55**, 1669
- Rubanenko, L., Venkatraman, J., & Paige, D. A. 2019, *NatGe*, **12**, 597
- Salvail, J. R., & Fanale, F. P. 1994, *Icar*, **111**, 441
- Sappington, J. M., Longshore, K. M., & Thompson, D. B. 2007, *The Journal of Wildlife Management*, **71**, 1419
- Schörghofer, N. 2022, *ApJL*, **927**, L34
- Schörghofer, N., & Rufu, R. 2023, *SciA*, **9**, eadh4302
- Schörghofer, N., & Williams, J.-P. 2020, *PSJ*, **1**, 54
- Schörghofer, N., & Williams, J.-P. 2024, *Icar*, **416**, 116086
- Schörghofer, N., Williams, J., Martinez-Camacho, J., Paige, D. A., & Siegler, M. A. 2021, *GeoRL*, **48**, e95533
- Schörghofer, N., Williams, J.-P., & Mazarico, E. 2024, *PSJ*, **5**, 126
- Schultz, P. H., Hermalyn, B., Colaprete, A., et al. 2010, *Sci*, **330**, 468
- Siegler, M., Paige, D., Williams, J.-P., & Bills, B. 2015, *Icar*, **255**, 78
- Smith, D. E., Zuber, M. T., Neumann, G. A., et al. 2010, *GeoRL*, **37**, L18204
- Spudis, P. D., Bussey, D. B. J., Baloga, S. M., et al. 2010, *GeoRL*, **37**, L06204
- Spudis, P. D., Bussey, D. B. J., Baloga, S. M., et al. 2013, *JGRE*, **118**, 2016
- Squyres, S. W., & Carr, M. H. 1986, *Sci*, **231**, 249
- Sridharan, R., Ahmed, S. M., Pratim Das, Tirtha, et al. 2010, *P&SS*, **58**, 947
- Sunshine, J. M., Farnham, T. L., Feaga, L. M., et al. 2009, *Sci*, **326**, 565
- Teodoro, L. F. A., Eke, V. R., & Elphic, R. C. 2010, *GeoRL*, **37**, L12201
- Teolis, B., Sarantos, M., Schörghofer, N., et al. 2023, *SSRv*, **219**, 4
- Thomas, R. J., Rothery, D.A., Conway, S. J., & Anand, M. 2014, *Icar*, **229**, 221
- Trask, N. J. 1966, *JPL Tech. Report 32-800*, 249
- Tye, A. R., Fassett, C. I., Head, J. W., et al. 2015, *Icar*, **255**, 70
- Tyler, R. H. 2021, *PSJ*, **2**, 70
- Vasavada, A. 1999, *Icar*, **141**, 179
- Venkatraman, J., Horvath, T., Powell, T. M., & Paige, D. A. 2023, *P&SS*, **229**, 105662
- Virkki, A., & Muinonen, K. 2016, *Icar*, **269**, 38
- Watson, K., Murray, B. C., & Brown, H. 1961, *JGR*, **66**, 3033
- Watters, T. R., Schmerr, N. C., Weber, R. C., et al. 2024, *PSJ*, **5**, 22
- Wilhelms, D. E., Howard, K. A., & Wilshire, H. G. 1979, *Geologic Map of the South Side of the Moon*, USGS, doi:10.3133/i1162
- Williams, J.-P., Greenhagen, B. T., Paige, D. A., et al. 2019, *JGRE*, **124**, 2505
- Williams, J.-P., Paige, D. A., Greenhagen, B. T., & Sefton-Nash, E. 2017, *Icar*, **283**, 300
- Williams, J.-P., Paige, D. A., Mahanti, P., et al. 2023a, *LPSC*, **54**, 1861
- Williams, J.-P., Paige, D. A., Siegler, M. A., & Martinez-Camacho, J. 2023b, *1st Workshop on Ices in the Solar System: A Volatile Excursion from Mercury and the Moon to the Kuiper Belt and Beyond*, 4039
- Williams, J.-P., & Rubanenko, L. 2024, *Ices in the Solar-System: A Volatile-Driven Journey from the Inner Solar System to its Far Reaches* (Amsterdam: Elsevier), 1
- Xiao, Z., & Werner, S. C. 2015, *JGRE*, **120**, 2277
- Xiao, Z., Zeng, Z., Ding, N., & Molaro, J. 2013, *E&PSL*, **376**, 1
- Yoldi, Z., Pommerol, A., Jost, B., et al. 2015, *GeoRL*, **42**, 6205
- Zhang, J. A., & Paige, D. A. 2009, *GeoRL*, **36**, L16203
- Zharkova, A. Y., Kreslavsky, M. A., Head, J. W., & Kokhanov, A. A. 2020, *Icar*, **351**, 113945